RESEARCH ARTICLE | FEBRUARY 15 2023

Mode interpretation and force prediction surrogate model of flow past twin cylinders via machine learning integrated with high-order dynamic mode decomposition

Tingting Liu (刘婷婷) ; Lei Zhou (周蕾) ; Hui Tang (唐辉) ; Hongfu Zhang (张洪福)

Physics of Fluids 35, 023611 (2023)
https://doi.org/10.1063/5.0138338

Physics of Fluids ARTICLE scitation.org/journal/phf

Mode interpretation and force prediction surrogate model of flow past twin cylinders via machine learning integrated with high-order dynamic mode decomposition

Cite as: Phys. Fluids **35**, 023611 (2023); doi: 10.1063/5.0138338
Submitted: 10 December 2022 · Accepted: 27 January 2023 ·
Published Online: 15 February 2023

Tingting Liu (刘婷婷),[1] Lei Zhou (周蕾),[2,a)] Hui Tang (唐辉),[3] and Hongfu Zhang (张洪福)[1]

AFFILIATIONS

[1]School of Civil Engineering, Northeast Forestry University, Harbin 150040, China
[2]Department of Civil and Environmental Engineering, The Hong Kong University of Science and Technology, Clear Water Bay, Kowloon, Hong Kong, China
[3]Department of Mechanical Engineering, The Hong Kong Polytechnic University, Hong Kong, China

[a)]Author to whom correspondence should be addressed: lzhouau@connect.ust.hk

ABSTRACT

Understanding and modeling the flow field and force development over time for flow past twin tandem cylinders can promote insight into underlying physical laws and efficient engineering design. In this study, a new surrogate model, based on a convolutional neural network and higher-order dynamic mode decomposition (CNN-HODMD), is proposed to predict the unsteady fluid force time history specifically for twin tandem cylinders. Sampling data are selected from a two-dimensional direct numerical simulation flow solution over twin tandem cylinders at different aspect ratios ($AR = 0.3$–4), gap spacing ($L^* = 1$–8), and $Re = 150$. To promote insight into underlying physical mechanisms and better understand the surrogate model, the HODMD analysis is further employed to decompose the flow field at selected typical flow regimes. Results indicate that CNN-HODMD performs well in discovering a suitable low-dimensional linear representation for nonlinear dynamic systems via dimensionality augment and reduction technique. Therefore, the CNN-HODMD surrogate model can efficiently predict the time history of lift force at various AR and L^* within 5% error. Moreover, fluid forces, vorticity field, and power spectrum density of twin cylinders are investigated to explore the physical properties. It was found three flow regimes (i.e., overshoot, reattachment, and coshedding) and two wake vortex patterns (i.e., 2S and P). It was found the lift force of the upstream cylinder for $AR < 1$ is more sensitive to the gap increment, while the result is reversed for the downstream cylinder. It was found that the fluctuating component of the wake of cylinders decreases with increasing AR at $L^* = 1$. Moreover, flow transition was observed at $L^* = 4$.

I. INTRODUCTION

In many engineering applications, groups of bluff bodies are more frequently observed than isolated bodies, such as twin decks or girders, linked buildings, offshore platforms, and solar plates.[1–4] Also, compared with flow motion around the isolated body, e.g., flow separation, reattachment, recirculation, and shear layer flapping, the flows around multiple bluff bodies are more complicated due to the interference effect of a neighboring building, and thus, their flow features are largely changed.[5–7] The vortex shedding formed behind bodies could generate unsteady forces and vibration on the bodies, which will bring a series of problems of structural safety, durability, and comfortability in practical engineering.[8] Therefore, it is of great significance to investigate the flow characteristics around multiple bluff bodies. In general, the arrangement of multiple bluff bodies is normally categorized into three different types: side-by-side, tandem, and staggered.[9] However, bodies in tandem arrangement present more complex flow properties than the other two conditions, and this is mainly because the downstream cylinder may submerge in the wake of the upstream cylinder and thus is affected by the wake vortex development from the upstream cylinder (e.g., vortex slapping, overshoot, and reattachment).[10] Moreover, wake interactions past multiple bluff bodies are common in practical engineering. Therefore, the need for a thorough understanding of the wake interaction mechanisms is gradually increasing to serve the flow control. For simplicity, twin cylinders

arranged in tandem are generally selected as the typically canonical model for investigating wake interaction.[6,11–13]

The flow over twin tandem cylinders and vortex shedding process has been extensively carried out in the literature, and most of them focused on simple regular structures (i.e., circular and square cross-sectional shapes).[14–20] Numerous studies have confirmed that the flow structures and aerodynamics forces of twin tandem cylinders are highly sensitive to the gap spacing ratio $L^* = L/D$, where L is the surface-to-surface distance between the twin cylinders and D is the characteristic dimension of the structure.[21–26] Based on the interaction behavior of shear layers of upstream and downstream cylinders, the flow regimes are classified into three by Igarashi[27,28] and Zdravkovich:[21] overshoot regime, reattachment regime, and coshedding regime. (I) The overshoot regime falls within the $0.5 < L^* < 1.0$, in which the shear layers separate from the upstream cylinder (UC) and overshoot the downstream cylinder (DC) due to the narrow gap. (II) The reattachment regime covers the $1.0 < L^* < 3.5$, in which the separated shear layers roll from the UC and reattach continuously onto the frontal surface of DC. (III) The coshedding regime prevails at $L^* > 3.5$, in which the two cylinders simultaneously generate vortices at the same frequency.[6,15,21,26] Moreover, critical gap spacing L^*_c is defined as a key quantity for the transition between reattachment and co-shedding regimes.[29,30] Alam and Meyer demonstrated that the coshedding flow is primarily occurred by the interaction between the gap vortices and the DC, whereas the reattachment flow is characterized by a strong interaction between the shear layers produced from UC and the DC.[31] Etminan *et al.*[14] studied the variation of fluid forces over twin tandem square cylinders in series at low Reynolds numbers. They observed that vortex shedding occurred at Reynolds numbers of 35–40. Zhou *et al.*[26] studied the flow characteristics of twin tandem circular cylinders in each regime based on flow structures in detail, including fluid forces, Strouhal number, and Reynolds number effects. Hu *et al.*[32] concentrated on the flow regimes of twin tandem circular cylinders with $Re = 2 \times 10^4$ and 3×10^6 at different gap spacings ($L^* = 2$–5) by means of numerical simulations. They noticed that for $L^* < 3.5$, the vortex street only develops behind the DC, while for $L^* > 3.5$, both the UC and DC shed vortices.

In engineering devices and systems, the cross-sectional dimensionality of the tandem structures is with various aspect ratios, such as twin-deck bridges, linked building, offshore, and bridge towers. Moreover, previous studies have found that, in addition to L^*, the length-to-width aspect ratio (AR) also plays an important role in determining the fluid force and flow field.[33–35] However, there is still an absence of investigation focusing on the flow properties of tandem cylinders simultaneously with different aspect ratios and gap spacing. Recently, Wu *et al.*[36] conducted numerical simulations of two elliptical cylinders in tandem with different gap spacings and AR in laminar flow. They found that after reaching the critical gap spacing, the fluid force of upstream decreases, and the downstream ones increase as AR increases. The flow properties show three regimes, namely, steady flow, shear layer attachment, and 2S or C(2S) shedding vortex. ul-Islam *et al.*[37] performed a numerical investigation to examine the effect of AR ($AR = 0.25$–1), L^* ($L^* = 0.5$–10), and Re ($Re = 75$–150) on the flow around twin tandem rectangles using the lattice Boltzmann method, yet their study focused only on $AR \leq 1$ and did not examine the key features and physical insight of the flow field.

As reviewed above, it is evident that the investigation regarding the effect of AR and L^* for flow regime transitions and the sensitivity of the fluid force of twin tandem cylinders is relatively insufficient. Moreover, the physical mechanism and fundamental features of the effect of AR and L^* on the flow dynamics around twin tandem cylinders are unclear, especially for rectangular cylinders. Thus, it is imperative to carry out a comprehensive study at various parameter cases to gain insight into the flow physics of tandem rectangular cylinders.

Coherent structures, which contain a significant amount of the total kinetic energy of turbulence, are organized motions enmeshed in turbulent flows.[38] Previous studies have demonstrated that knowing the development and unique morphologies of coherent structures is beneficial in identifying the underlying physical mechanics of the flows.[8,39] As a result, it has been tremendous efforts to extract the physically significant features and modes from the flow data. One of the methods, dynamic mode decomposition (DMD), is widely adopted to identify the flow features. It can be applied to extract spatial structures with eigenfrequencies and growth or decay rates, as well as to obtain approximations of Koopman patterns and eigenvalues of the fundamental system.[40] Many variants are derived from DMD, one of which, high-order dynamic mode decomposition (HODMD), gives a higher accurate estimate of the system's eigenvalues with small residuals and is suitable for highly nonlinear systems in complex flow compared with the standard DMD.[41] So far, few scholars have applied the HODMD to the study of flow past twin tandem cylinders to gain insight into spatial morphology and temporal evolution feature of the flow physics essence.

Furthermore, the coherent structural behavior of laminar and turbulent flows has similar features mainly due to the underlying 2 D nature of the vortex shedding.[42,43] This suggests that research on laminar flows could explain the more complicated vortex shedding phenomena in a turbulent flow. Subsequently, the properties of the underlying physical mechanism of the turbulent flow field for bluff bodies can be both quantitatively and qualitatively exposed by investigating the turbulence variations at low Reynolds numbers (e.g., $Re < 200$).[6]

In addition, rectangular structures arranged in tandem have a wide range of parameters in terms of gap spacing and aspect ratio. Possible combinations of these factors are too many that not all cases can be considered in the research. Therefore, it is necessary to develop the development of a surrogate model to predict the fluid forces of twin tandem rectangular cylinders, which can be of significant benefit for the design of engineering structures.

With the rapid development of data science and computational capability, machine learning becomes powerful tools to mine useful information from massive data accumulated in engineering, thereby providing effective guidance for summarizing new physical pattern.[44–46] With respect to fluid mechanics, recently, convolutional neural networks (CNNs) achieve good performance in the flow field reconstruction of flows past bluff bodies. Zhao *et al.* used neural networks (NNs) to train a large amount of flow field data around a cylinder with external constraints in order to reconstruct the velocity field and fluid forces.[47] They found that convolutional neural networks perform well in predicting flow fields and forces at complex boundaries, and have the advantage of high predictive efficacy and accuracy. Bhatnagar *et al.* used CNNs to build an approximate model to predict the velocity and pressure fields around different airfoil geometries under different flow conditions.[48] The results showed that CNNs are robust in accurately identifying the relevant subspaces, with a

maximum error of 26% for surface loads. Miyanawala and Jaiman used CNNs to predict unsteady the force coefficients of bluff bodies with different shapes at low Reynolds numbers and performed a systematic sensitivity and convergence investigation to determine the effective dimensions of the process of CNNs for deep learning. Their results successfully confirmed the predictive capability of CNNs for force coefficients of blunt bodies.[49]

From the above-mentioned research results, it can be seen that the researchers only predicted the statistical value (e.g., mean and RMS) of drag-and-lift forces of the bluff bodies and failed to focus on the temporal evolution of force, i.e., the time history of the force. In fact, compared to mere statistical properties, full history of the fluid force in temporal contains more fruitful and profound information; thus, understanding force development over time is extremely important for gaining insight into underlying physical laws of the flow field. Furthermore, modeling the time history of forces contributes to the construction of the surrogate reduced-order model, which could greatly reduce the computational cost compared with the traditional computational fluid dynamics (CFD). Subsequently, this undoubtedly promotes to realize calculating, controlling, and predicting of aerodynamic feature of fluid–structure coupled dynamic system with a real-time adaptive and close-loop feedback manner. Hitherto, barely any previous studies, to the best knowledge of authors, have combined HODMD and CNN to the application of predicting the time history of unsteady fluid forces for bluff bodies, particularly for twin tandem cylinders. With respect to twin tandem cylinders, in view of its universality in engineering application and complexity in scientific mechanism, it is very necessary to study the influence of two important internal parameters, i.e., aspect ratio and gap spacing, on the aerodynamic feature and the involved fundamental physical laws.

Hence, in the present study, a new method, CNN-HODMD technique, is proposed to establish a surrogate model for predicting the time history of unsteady force based on the input parameters (AR and L^*) for flow past twin tandem cylinders. The purpose is to demonstrate the good performance of this technique for predicting fluid forces and its high potential to be used as a reduced-order model for extrapolation.

To examine the effect of length-to-width aspect ratio (AR) and gap spacing qualitatively and quantitatively (L^*) on the fluid force and flow regime, a parametric analysis is conducted for the direct numerical simulation (DNS) flow solution over twin tandem cylinders in a range of $AR = 0.3$–4 and $L^* = 1$–8 at $Re = 150$. To understand the correspondence between load feature and flow field, synchronous mode decomposition analysis on pressure and velocity field is undertaken via HODMD.

The HODMD method was applied for two different levels and purpose in this study (1) to augment and extract the mode coefficients of the fluid force for the preparation of developing the mode-based force-prediction surrogate model; (2) to capture the spatial morphology and temporal evolution feature of the flow field at typical flow regimes, so as to provide physical interpretations of the fluid force characteristics and the machine learning prediction results at different input parameters (AR and L^*).

II. NUMERICAL METHODOLOGY AND SURROGATE MODEL

A. Direct numerical simulation (DNS)

The two-dimensional time-dependent Navier–Stokes equations were solved in a Cartesian reference system attached to twin tandem rectangular cylinders to obtain the flow solution. The system is assumed to be incompressible, Newtonian, unstable, and laminar flow. Thus, the 2D Navier–Stokes equations for this fluid flow can be expressed as follows:

$$\frac{\partial \mathbf{u}}{\partial t} = -(\mathbf{u}\cdot\nabla) - \nabla p + \frac{1}{Re}\nabla^2\mathbf{u}, \tag{1}$$

$$\nabla\cdot\mathbf{u} = 0, \tag{2}$$

where p denotes the pressure and $\boldsymbol{u}$ denotes the instantaneous velocity vector. All physical variables are guaranteed to be dimensionless by the inlet velocity (U) and rectangular cylinder width (D).

The present work considers the system with twin stationary cylinders in a tandem arrangement. The setting and layout of the numerical calculation are shown in Fig. 1. Herein, two rectangular cylinders are separated by the surface-to-surface distance L; the non-dimensional parameter L^* ($L^* = L/D$) is referred to as the gap spacing ratio and used hereafter. To simplify the investigated problem, two cylinders are identical in width D but with different lengths B. The aspect ratio of a rectangular cylinder is defined as $AR = B/D$. The upstream cylinder is exposed to a uniform free flow (U) at $Re = 150$, while the downstream one is submerged in its wake. Aspect ratio scenarios of twin cylinders include $AR = 0.3$, 0.5, 1.0 (square), 2.0, 3.0, and 4.0 (from slender to flat), and the dimensionless gap ratios contain $L^* = 1$, 2, 3, 4, 6, 8. N–S equations were solved using the finite volume method by the implicit pressure-based solver in ANSYS-Fluent 17.0. Here, the third-order MUSCL scheme was employed to discretize the convective term. Implicit second-order scheme was used to handle time-advanced term.

As can be seen in Fig. 1(a), the coordinate origin is located at the center of the upstream cylinder, and the distance between the upper/lower boundaries and the centerline of the computational domain is 15 D. The maximum blockage ratio is 3.3%. The two-dimensional view of quadrilateral grid distributions around the cylinders and detail enlargements is shown in Fig. 1(b). It can be noted that, to better capture the complex flow phenomena around the twin cylinders, the grid is encrypted near the cylinder surface. We impose a Dirichlet boundary condition (BC) ($u = U$, $v = 0$) at the inlet of the computational domain and a pressure outlet BC at the outlet. Here, u and v represent the velocity components in the x and y directions, respectively. Symmetric boundary conditions were applied to the upper and lower sides, and no-slip wall boundary conditions ($u = 0$, $v = 0$) were adopted on the surface of twin cylinders.

B. CNN-HODMD force prediction model

1. Convolution neural network (CNN)

CNN models perform well in automatic feature learning and extraction from data; thus, its generalization capability is better than traditional approaches. The main components of the network structure include input layer, convolution layer, pooling layer, full connection layer, and output layer. In this paper, the CNN is designed for predicting the time history of lift force coefficient for twin tandem rectangular cylinders. In this paper, multi-convolutional layer is used and the nonlinear activation function $ReLU$ is added to the convolution process. The convolution layer is calculated as follows:

$$y_c = ReLU(\kappa \times x_c + b_c), \tag{3}$$

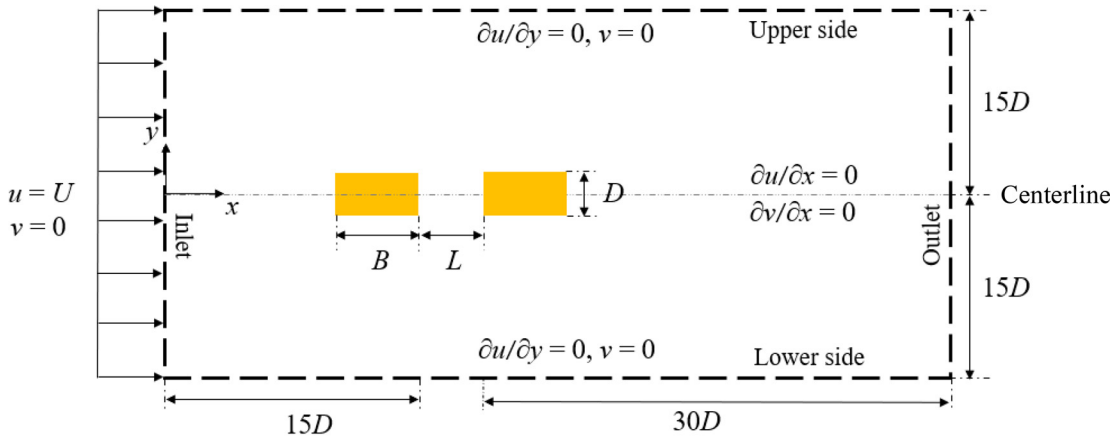

(a) Computational boundary conditions

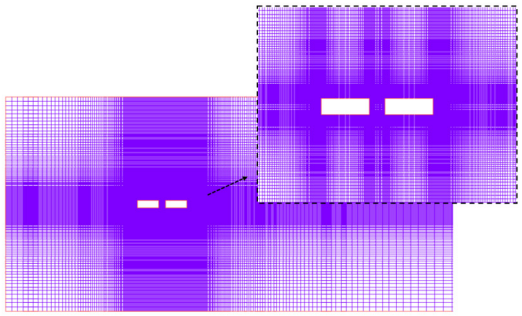

(b) Global mesh and lobal close-up mesh around the twin tandem cylinders.

FIG. 1. Computational boundary conditions and mesh scheme.

where *ReLU* stands for the nonlinear activation function, κ denotes convolution kernel, x_c represents the input mode coefficients extracted from the higher order DMD, and y_c stands for the output of the convolution layer. The max pooling layer is set after the activation layer in order to reduce the dimensionality to prevent overfitting, as shown in Fig. 2(a). The fully connected layer links all the components before that layer and reduces the output two-dimensional data from the convolution and pooling layers into a one-dimensional vector, denoted as follows:

$$y_f = w_f x_f + b_f, \tag{4}$$

where x_f and b_f represent the input data and output data of the fully connected layer, respectively, and w_f denotes the weight. The excitation function *ReLU* for each neuron was employed in the fully connected layer to enhance the performance of the convolutional neural network. To improve the overfitting impact brought on by training complicated feedforward networks on relatively limited datasets, the dropout layer is introduced in this study. The formulas are as follows:

$$\begin{aligned} r_j^l &\sim Bernoulli(p), \\ \tilde{y}^l &= r^l * y^l, \\ z_i^{l+1} &= w_i^{l+1}\tilde{y}^l + b_i^{l+1}, \\ y_i^{l+1} &= f(z_i^{l+1}), \end{aligned} \tag{5}$$

where r is a probability vector generated by the Bernoulli function, i.e., a random vector of 0 or 1. y^l and $\tilde{y}^l$ represent the input data of this layer and the input data to filter out some neurons, respectively. The sparse matrix is built by dropout layers so that a certain neuron stops operating with probability p. To prevent some features from being effective only when combined with other specific features, the updating of weights no longer depends on the joint activity of hidden nodes with defined relationships, which allows the network to learn features more robustly. The network structure of the CNN model is shown in Fig. 2(b).

2. Higher-order dynamic mode decomposition (HODMD)

The dynamic model decomposition method, based on Koopman theory, is a data-driven method that can be used to model and can

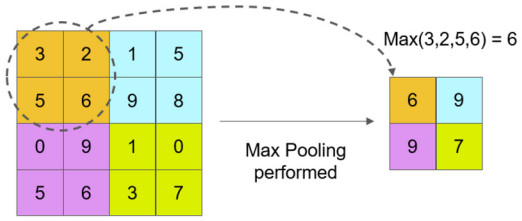

(a) Demonstration of maximum pooling

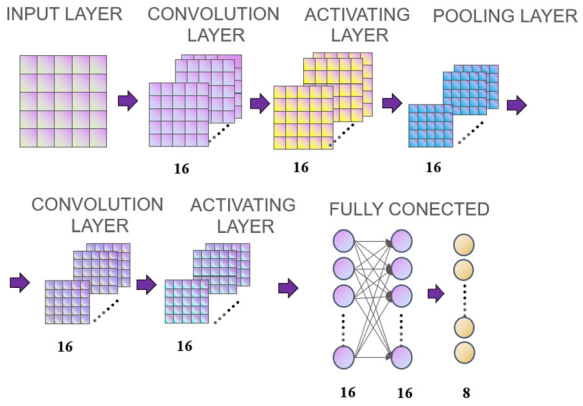

(b) Network structure of the CNN model

FIG. 2. Demonstration of maximum pooling (a) and network structure of the CNN model (b).

linearly approximate high-dimensional dynamic systems. DMD has many improved variant methods, HODMD is one of the advancements of standard DMD, and it has good performance in extracting the essential features of complex nonlinear turbulent systems by augmenting the dimensionality of observable variable, especially for those dynamic systems with noise interference and mismatched time–space dimensions. Here, the general processes are only illustrated, and for more details of the algorithm, the reader is referred to the investigation of Wynn *et al.* Based on Koopman's assumption, the snapshot image matrix $U_{N\text{-}1}$ at the previous instant can be mapped to the matrix U_N at the subsequent instant by means of introducing a best-fit linear mapping system A and a residual matrix R, which can be expressed as follows:

$$AU_{N-1} = U_N + R, \tag{6}$$

$$U_{N-1} = [u_1, u_2, u_3, \ldots, u_{N-1}], \tag{7}$$

$$U_N = [u_2, u_3, u_4, \ldots, u_N]. \tag{8}$$

The optimal problem is solved to identify the low-dimensional subspace, i.e., minimizing the residual R to find the best mapping approximation. The minimization problem can be expressed as follows:

$$\min\|U_N - AU_{N-1}\|^2 = \min \sum_{i=1}^{N} \|u_{i+1} - Au_i\|_2^2, \tag{9}$$

such that

$$L^T L = I, \quad M \in R^{r\times r}, \quad L \in R^{p\times r}, \tag{10}$$

where $\|\cdot\|_2$ represents the Frobenius matrix norm, and r stands for the rank of operator matrix $A = LML^{\mathrm{T}}$, which is typically smaller than p. Here, to estimate the initial dynamical system, the low-order dynamics $A = LML^{\mathrm{T}}$ is introduced. The expression for the rank constraint of Eq. (11) can be derived as follows:

$$\min\|U_N - LML^T U_{N-1}\|^2, \tag{11}$$

$$M \in R^{r\times r}, \quad L \in \{R^{p\times r} | L^T L = I, k < p\}, \tag{12}$$

where the low-dimensional subspace is denoted by L, in which each column of L is an orthogonal basis explaining the shape of the eigenmodes, and M is a projection operator that gives a linear approximation to the evolution. The objective is to construct optimal variables L and M to minimize the parametrization in Eq. (12). Thus, solving the two variables, minimization issue is not easy. Wynn *et al.* argued that the minimization problem can be solved by using manifold flow optimization techniques. The optimization problem can be rewritten as follows:

$$\max g(L) = \|L^T U_N Q(L)\|^2, \tag{13}$$

such that

$$L \in \{R^{p\times r} | L^T L = I, k < p\}, \tag{14}$$

$$Q(L) = U_{N-1}^T (L^T U_{N-1} L)^{-1} L^T U_{N-1}. \tag{15}$$

In the sense of least squares, the optimal low-order space subbasis L_i and the optimal linear dynamics on the corresponding space $\mathrm{M}(L_i)$ can be attained. The logarithmic expression of the eigenvalues of DMD is

$$\lambda_i = \frac{\log \mu_i}{\Delta t}, \tag{16}$$

where μ_i is the eigenvalue of the matrix M. The real part of λ_i can determine the stability in time by offering a growth rate, while the virtual part indicates the mode's frequency. The associated dynamic model φ_i, which corresponds to the determined value of λ_i, is written as

$$\varphi_i = Ly_i, \tag{17}$$

where y_i is the eigenvector of the matrix M. The projection parameter α_i represents the amplitude of the corresponding mode:

$$\alpha_i = (\varphi^{-1})_{ij} (u_1)_j. \tag{18}$$

For each mode, the energy E_i can be presented as the product of the mode and the according projection parameter

$$E_i = |a_i \varphi_i|. \tag{19}$$

The mth original flow field can be reconstructed as follows:

$$u_m = \sum_{i=1}^{n} a_i \varphi_i \lambda^{m-1}. \tag{20}$$

However, the standard DMD is not suitable for highly nonlinear systems, especially for the case in which spectral and spatial complexity frequently do not match with each other. Consequently, HODMD is developed to supplement the situation of the highly nonlinearized

system. The underlying theory of HODMD is Taken's delay embedding theorem, which can augment the dimensionality of observed variables. Thus, with the assistance of HODMD, the observation original matrix V_1^K is extended to matrix $\overline{V}_1^{K-d+1}$ with a desirable dimension by adopting d index-lagged snapshots as expressed in Eq. (22). Note that $\overline{V}_1^{K-d+1}$ is the sub-matrices formed with the first $K-d$ columns and the last $K-d$ columns of the modified snapshot matrix. Then, $\overline{V}_1^{K-d+1}$ is applied as input data, while the remaining steps are consistent with DMD, which is referred to HODMD in this study

$$V_1^K = [v_1, v_2, \ldots, v_k, v_{k+1}, \ldots, v_{k-1}, v_k], \tag{21}$$

$$\overline{V}_1^{K-d+1} = \begin{bmatrix} V_1^{K-d+1} \\ V_2^{K-d+2} \\ \cdots \\ V_{d-1}^{K-1} \\ V_d^K \end{bmatrix}. \tag{22}$$

3. CNN-HODMD model

The basic idea of the CNN-HODMD model is to use the mode coefficients that are extracted by HODMD that can reconstruct the original flow field as the input data, and by means of CNN, with the training of a large number of data sets, enabling to develop an appropriate model that can predict the mode coefficients of the flow field for a given AR and L^*. The predicted mode coefficients can be used to reconstruct the time history of forces in the corresponding case. The training and testing process of the CNN-HODMD model are shown in Fig. 3. The detailed process is as follows:

For the training process:

First, numerical simulations or experiments are used to obtain the aerodynamic forces of the twin tandem cylinders with different parameters of AR and L^* (in this paper, lift force is used as the original data). Next, the modal coefficient vector is calculated using the HODMD method by decomposing the various aerodynamic forces. Finally, the surrogate model is created by training with CNN using the parameters AR and L^* as inputs and the modal coefficients as outputs.

For the testing process:

First, we input the new parameters of AR and L^*, and the HODMD modal coefficients are calculated using the well-trained surrogate model. Following that, the time history of aerodynamic force is predicted by using multi-order modal coefficients as well as comparing with CFD calculation results.

It should be noted that the entire training and testing process is based on HODMD coherent mode-aid (physical interpretation aid). The necessity is that most of the studies in the past were focused on predicting the mean and fluctuating force of structures, while this paper is devoted to predicting the time history of aerodynamic force, which contributes to develop the reduced-order model of fluid–solid coupling quickly.

The aim of the CNN-HODMD training is to reduce the loss function. In this paper, the root mean square error (RMSE) is used as the loss function in CNN-HODMD models, denoted as follows:

$$RMSE(y, y') = \sqrt{\frac{\sum_{i=1}^{n} (y_i - y_i')^2}{n}}, \tag{23}$$

where y_i is the original value of the ith batch of data, and y_i' is the predicted value of CNN.

III. VERIFICATION AND VALIDATION

The grid and time steps of independence verification result for $Re = 150$ are given in Table I. Three different types of meshes

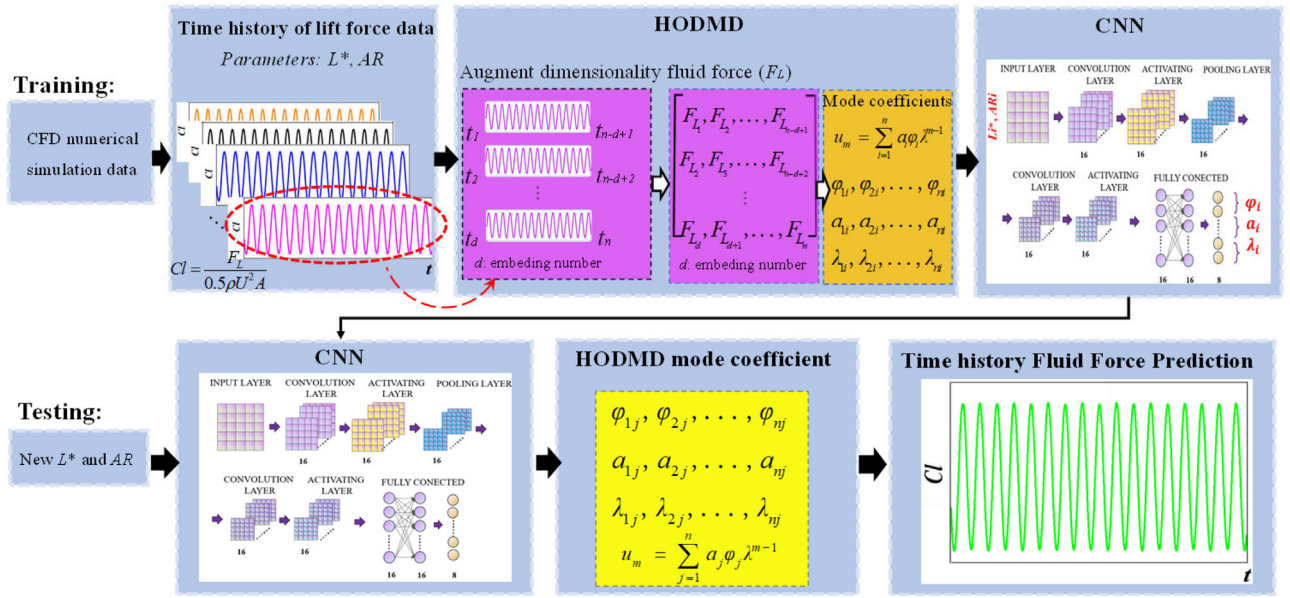

FIG. 3. Training and testing process.

TABLE I. Verification of mesh and time step independence for twin tandem cylinders ($Re = 150$, $L^* = 1$, $AR = 1$).

Scholar	Number of nodes	Time step	St(UC)	Cl'(UC)	Cd(UC)	St(DC)	Cl'(DC)	Cd(DC)
Present	25 623	0.008	0.140	0.015	1.297	0.140	0.042	−0.192
	34 333	0.005	0.140	0.015	1.312	0.140	0.040	−0.204
	59 013	0.001	0.142	0.014	1.295	0.142	0.040	−0.192
Sohankar[50]		⋯	0.140	0.014	1.290	0.140	0.042	−0.190
Nikfarjam *et al.*[51]		⋯	0.136	⋯	1.286	0.136	⋯	−0.200

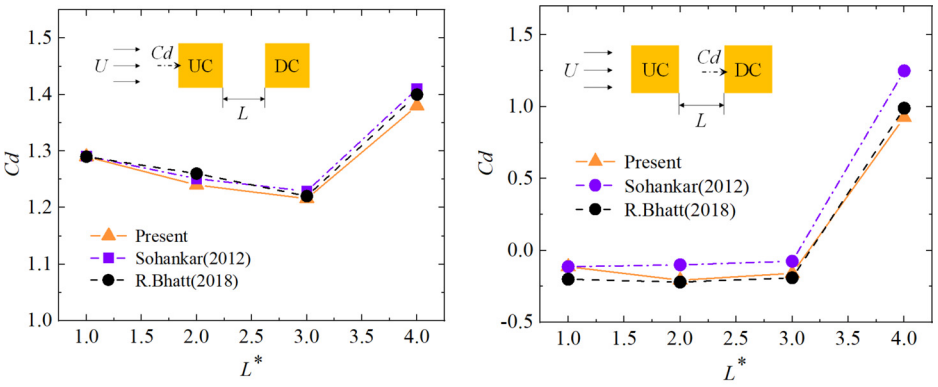

FIG. 4. Comparison of mean drag coefficients for twin cylinders at different values of L^* for $Re = 150$.

(i.e., coarse, medium, and fine mesh) were tested at $\Delta t = 0.008$, 0.005, and 0.001, respectively. The aerodynamic force results for UC and DC were calculated for these three cases and compared with those provided in the previous literature, including the mean drag coefficient (Cd), fluctuating (RMS), lift coefficient (Cl'), and Strouhal number (St, $St = fD/U$). Note the force coefficients were dimensionless with $1/2\rho U^2 D$, where ρ represents the air density and U denotes the free flow velocity. Table I shows the comparison of the grid and time step-independent validation results with previous studies. As can be seen in Table I, merely slight differences were found among five cases. Therefore, to balance the efficiency and accuracy of the numerical calculation, medium mesh and $\Delta t = 0.005$ were selected and applied in the subsequent study to compute the results of the forces and flow fields.

Figure 4 compares mean drag coefficient Cd of two tandem square cylinders at different gap spacing ratios L with the results in Sohankar[50] and Nikfarjam.[51] It is evident that the present simulation results are in good agreement with previous studies. At $3 < L^* < 4$, an abrupt jump in Cd is observed for both cylinders, which may be due to the occurrence of a transition in the flow field regime. For precautionary purposes, a comparison of the mean drag coefficients was performed between former study and the present study for single cylinders with two different aspect ratios (i.e., $AR = 1$ and 4), as shown in Table II. The results of current study well agree with those of Mashhadi,[33] which again verifies the accuracy of this numerical scheme adopted in this study.

IV. RESULTS AND DISCUSSION

A. CNN-HODMD model prediction

In order to examine the performance of the HODMD method in reconstructing time history of fluid force, two representative cases are selected here for testing by comparing with the original data. Figs. 5(a) and 5(b) show the comparison of the original Cl time history of DC with that of DC reconstruction results obtained by the first two orders, the first four orders, and the first eight orders of HODMD mode coefficients, respectively, for two different tandem cylinders scenarios, i.e., $L^* = 8$, $AR = 0.3$ and $L^* = 8$, $AR = 2$. In general, the time history of Cl can be well reconstructed using the first four and first eight orders of HODMD mode coefficients. However, it is observed that the curves reconstructed from the first two orders of modes differed significantly from the original data curve at $L^* = 8$, $AR = 0.3$. Also, for $L^* = 8$, $AR = 2$, this maximum error reaches 1.2%, while the maximum error of the curves reconstructed with the first four and first eight orders of mode coefficients are less than 1%. This indicates that the nonlinear characteristics of the dynamical system of the tandem cylinders are significant, resulting in higher-order modes also occupying a relatively important role.

Therefore, the modal coefficients extracted from the first four orders of HODMD are used in all cases as the input data for the CNN

TABLE II. Comparison of the results of a single cylinder between the present study and earlier literature ($Re = 150$, $AR = 1$, 4).

Scholar	AR	Cl'	Cd	St
Present	1	0.280	1.438	0.157
	4	0.105	1.105	0.137
Mashhadi	1	0.269	1.466	0.162
	4	0.114	1.148	0.140

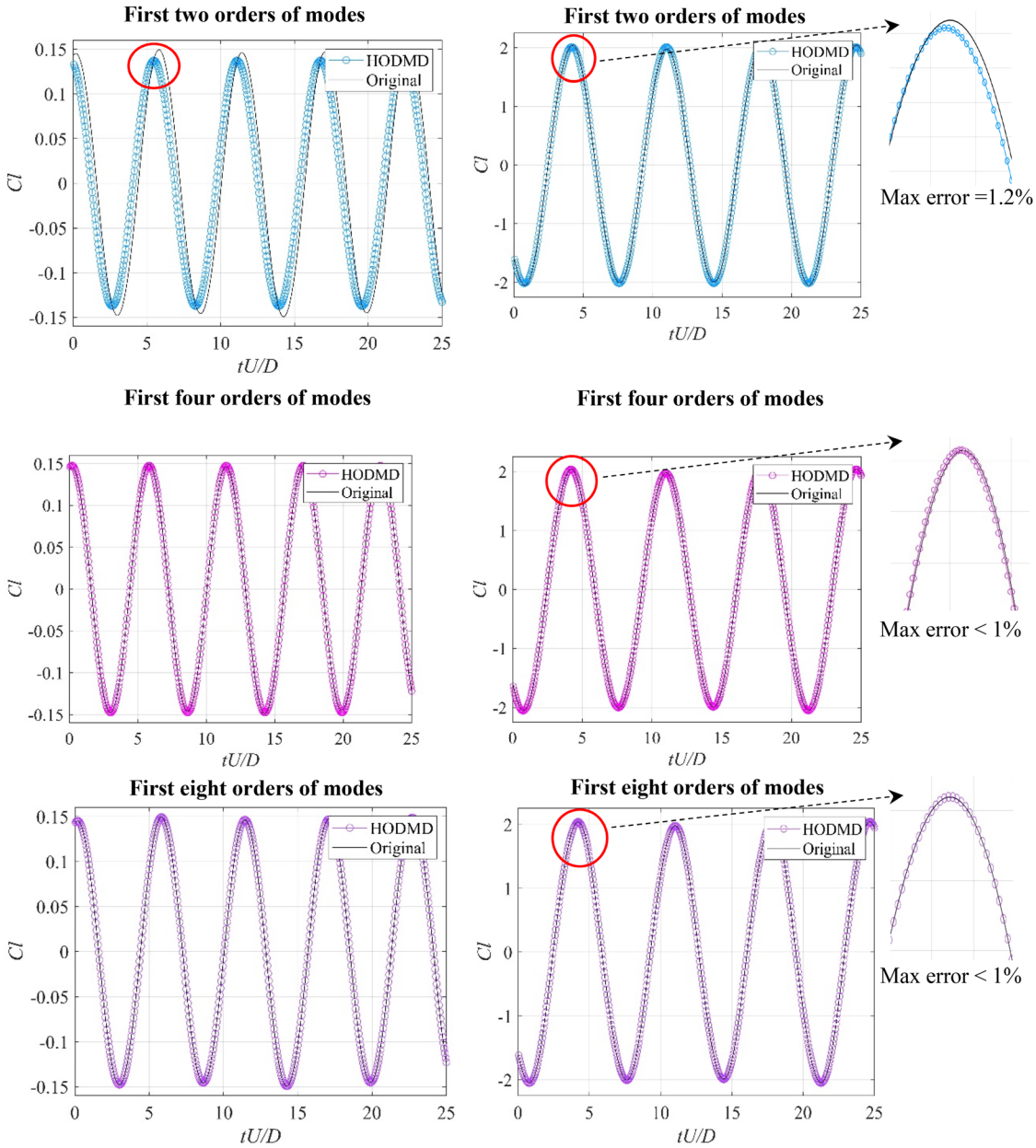

FIG. 5. Comparison of the original *Cl* time history of DC with that of reconstructed results from the first two orders, the first four orders, and the first eight orders of HODMD mode coefficients for two different cases $L^* = 8$ $AR = 0.3$ (a), and $L^* = 8$ $AR = 2$ (b).

in order to train a suitable model for predicting the time history of *Cl*. Using 135 groups, L^* varies from 1 to 8 with an interval of 0.5, each L^* corresponding to 9 *AR*s, $AR = 0.3$, 0.5–4 with an interval of 0.5, respectively. The neural network was trained based on 80% original data that are randomly selected to accurately predict the *Cl* time history of DCs under certain *AR*s and L^*. To verify the accuracy of the trained surrogate model CNN-HODMD, the *Cl* time history of the rest of 20% original data is employed for testing. Herein, only the load prediction curves for six different cases (i.e., $L^* = 4$, corresponding to $AR = 0.3$, 0.5, 1, 2, 3, 4, respectively) were exhibited and compared the true simulated results.

The CNN-HODMD model is trained by using the Adam optimization algorithm and the Error backpropagation algorithm. The curves of root mean square error (RMSE) and loss of the training process at

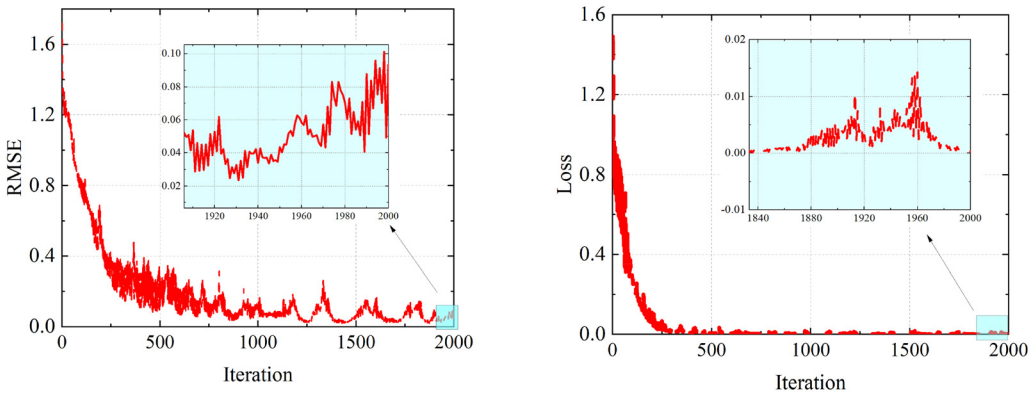

(a) RMSE curve (b) Loss curve

FIG. 6. RMSE and loss curves of the training process.

$L^* = 4$ $AR = 3.0$ are displayed in Fig. 6. Due to the complexity of the network structure of the CNN-HODMD model, the curves of RMSE and loss decrease relatively slowly and stabilize as the number of iteration steps increases. As observed from the enlarged plots of Fig. 6, the RMSE curve decreases to below 0.1 and the loss curve decreases to below 0.02, which indicates a high precision of the training process. For simplicity, the training process for the other cases is not described here. Figure 7 shows the RMSE values of the mode coefficients for the six testing cases. The RMSE value keeps within 0.01, which demonstrates the high accuracy of the CNN-HODMD model for modal coefficient prediction. In addition, the accuracy of the mode coefficients for $AR > 1$ is higher than that for $AR < 1$, which is possibly because the flow regimes experience a distinctive change of the twin cylinders for $L^* = 4$, $AR < 1$. The relevant variation in flow field with aspect ratio will be described in the Secs. IV B and IV C, and explained in detail by mode decomposition analysis in Sec. IV D.

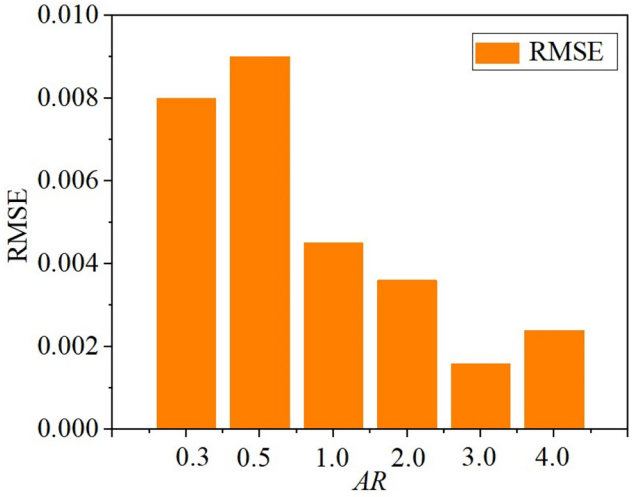

FIG. 7. RMSE of six testing cases ($L^* = 4$, $AR = 0.3, 0.5, 1.0, 2.0, 3.0, 4.0$).

Figures 8(a)–8(d) show the predicted results of time-history lift force coefficient curves of UC and DC for $AR = 0.3, 0.5, 1.0, 4.0$ at $L^* = 4$, and they are compared with the original load curves sampled from the fully developed flow. As can be seen, after the flow field becomes stabilization, the lift curve of both the UC and the DC behaves as a regular sinusoidal function. The Cl time history predicted by CNN-HODMD surrogate model matches well with the original data results for all four different AR cases, albeit with some small errors. Overall, with the increase in AR, the error increases slightly, but it is still less than 5%. This indicates that the CNN-HODMD model can well capture the potential relationship between the time history of lift force of the twin tandem cylinders and the input parameters.

Moreover, these figures clearly show that the magnitude of the fluid force on the twin cylinders intimately depends on the aspect ratio. For $AR \leq 1$, as AR increases, the amplitude of lift on the DC gradually increases compared to the UC, and the lift on twin cylinders gradually changes from anti-phase to in-phase, which is consistent with the findings of ul-Islam.[37] Notably, the lift of UC and DC decreases significantly when AR increases 4, which may be related to the transition in behavior of the shear layer and the vortex shedding pattern for the cylinder with a relatively long afterbody.

B. Fluid forces and flow structures

As is known that machine learning always lacks physical interpretation. Because we have embedded the physical mode decomposition method HODMD, the proposed CNN-HODMD model has physical interpretation to some extent. Once the fluid force is decomposed by HODMD, it is oscillating that amplitude and frequency can be represented by mode coefficients in the sense of Fourier expansion. On the other hand, we can decompose the flow field in the same way, and thus, we build a correspondence between fluid force and flow field. In other words, we can give physical interpretation of mode coefficients by using the coherence modes of flow field. To further confirm the validity and increase physical interpretability of machine learning results, in Secs. IV C and IV D, the characteristics and latent mechanisms of fluid forces and flow field are presented.

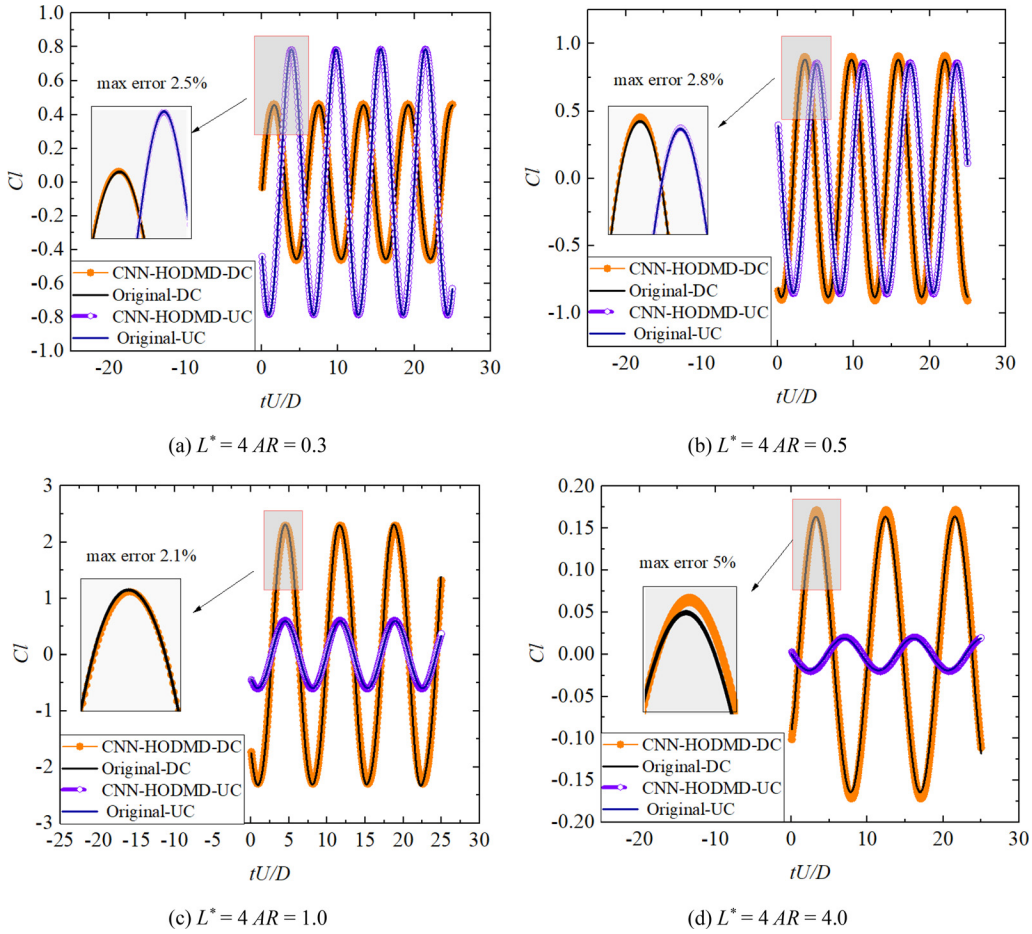

FIG. 8. Comparison of time history of lift force coefficient of UC and DC between the predicted results by CNN-HODMD model and original curves for $AR = 0.3$, 0.5, 1.0, 4.0 at $L^* = 4$.

Figure 9 shows the contours of the fluctuating lift coefficients (Cl') and mean drag coefficients (Cd) of DC and UC of various L^* and AR cases. It can be observed that the fluid force of the twin tandem cylinders is highly dependent on the gap spacing L^* and AR. Here, based on the variation pattern of the contours, gap spacing cases are classified into three different types, namely, small gaps ($L^* = 1$, 2), medium gaps ($L^* = 3$, 4), and large gaps ($L^* = 6$, 8). Figures 10–12 illustrate the instantaneous vorticity, time history of lift coefficient, and the associated power spectrum density (PSD) at three representative gap spacing cases, i.e., $L^* = 1.0$, $AR = 0.3$; $L^* = 4.0$, $AR = 1.0$; and $L^* = 8.0$, $AR = 2.0$, which corresponds to the small gap, medium gap, and large gap, respectively.

In general, the fluctuating lift reflects the strength of the vortex shedding, as shown in Figs. 9(a) and 9(c). According to the magnitude of fluctuating lift, the flow state can be classified into 3 categories (split by yellow lines), namely, no vortex shedding, weak vortex shedding, and strong vortex shedding. For small gaps ($L^* = 1$, 2), weak vortex shedding occurs on the UC and DC for $AR \leq 1$; however, it disappears with $AR > 1$. The reason is that the rectangular cylinder with $AR < 1$ resembles a slender plate, which easily rolls up vortices on the leeward side. An interesting finding that can be observed from Figs. 9(b) and 9(d) is that the mean drag force applied to DC is smaller than that of UC in all selected ranges, especially when $AR \leq 1$, the mean drag force applied to DC is negative. Furthermore, it can be seen from Fig. 10(a) that the shear layer of UC overshoots the DC with no vortex shedding appearing in the gap at $AR = 0.3$. It indicates that the presence of DC suppresses the vortex shedding of UC when two cylinders are arranged in tandem with small gap ratio. In Fig. 10(b), it is observed the existence of primary peak that indicated vortex shedding frequency and other smaller harmonics, where the highest peak indicates the primary vortex shedding frequency and the other sub-/superharmonics that represents the nonlinearity of the flow field. For $L^* = 1.0$, $AR = 0.3$, the subharmonic peaks of the DC are much lower than the primary spectral peak, presenting single frequency spectrum feature.

For large gaps ($L^* = 6$, 8), strong vortex shedding occurs at $AR < 1$ for UC, while it appears at $AR > 1$ for DC. It is because the interference of the wake of UC to the DC is relatively small for $AR < 1$; however, this effect is strengthened and thus enhanced the vortex shedding strength of DC as the AR increases. This speculation is confirmed by the flow motion as shown in Fig. 12(a). As can be

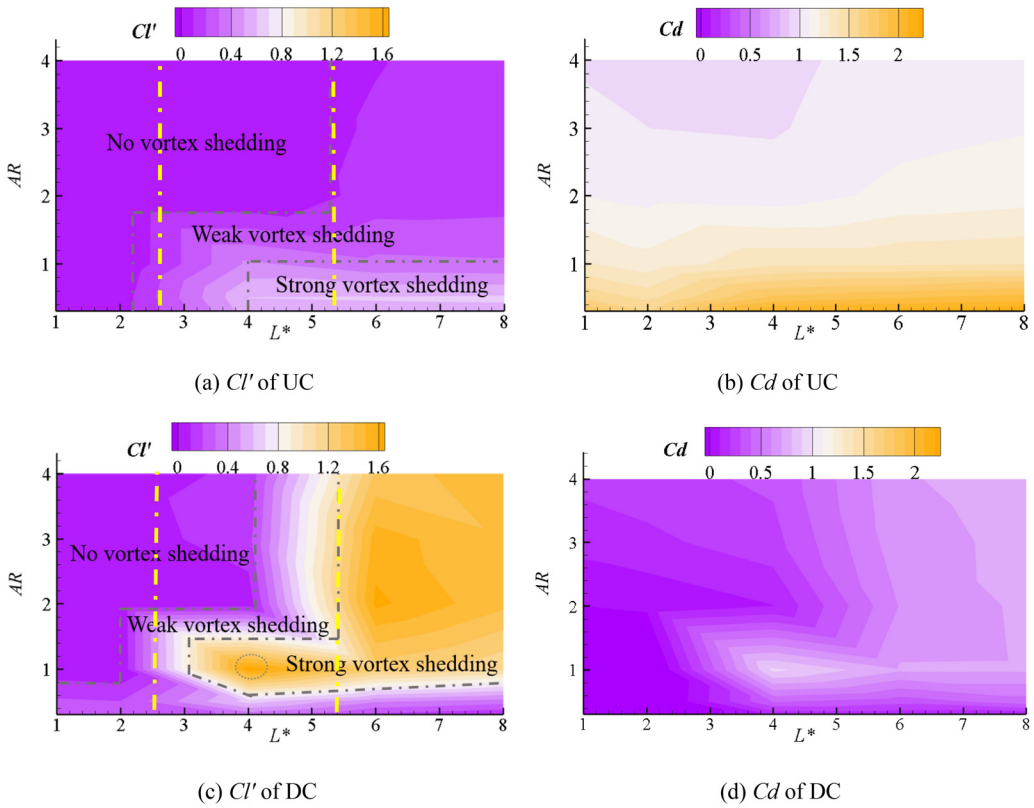

(a) *Cl′* of UC (b) *Cd* of UC

(c) *Cl′* of DC (d) *Cd* of DC

FIG. 9. Fluid force coefficients as a function of *AR* for different L^*.

seen, the DC for $L^* = 8.0$, $AR = 2.0$ was submerged in the wake of UC and was continuously slapped by the shear layer separated from the UC. Moreover, with the increase in *AR*, the presence of DC inhibits the development of the wake of UC, resulting in the flow transition from strong vortex shedding to weak vortex shedding.

In addition, the mean drag of UC and DC is not significantly dependent on the gap spacing. However, the effect of *AR* on the mean drag of UC was significant. As *AR* increases, the mean drag of UC gradually decreases. This means that the flat cylinder is subject to less drag force than the slender cylinder for the UC. In Fig. 12(b), there are multiple spectral peaks near the low frequency at large gaps, which indicates the fluctuation instability and complexity of the wake of DC. Compared to the small gaps, the PSD value of the primary frequency for large gap case is dramatically increased (PSD from 21.68 to 810), which implies the enhanced energy of vortex shedding. For $L^* = 8.0$, $AR = 2.0$, behind the twin rectangular cylinders, the vortex evolves simultaneously to a fully developed co-shedding flow regime as shown in Fig. 12(a).

For medium gaps ($L^* = 3, 4$), the fluctuating lift coefficient of UC and DC is almost equal to that of large gaps when $AR < 1$, and to that of narrow gaps when $AR > 1$. It is noteworthy that a sudden jump for *Cl'* is observed at $AR = 1$ of DC, which indicates that the gap flow has the strongest effect on the DC, causing a sharp peak in the vortex shedding strength of the DC. In Figs. 11(a) and 11(b), the shear layer separated from the UC is reattached to the DC, which is accompanied by a high-energy primary frequency fluctuation. Moreover, the primary frequency of the medium gap decreases (*St* from 0.17 to 0.14), which implies an increase in the vortex shedding scale.

C. Flow regime dependence on L^* and *AR*

Aiming to summarize the geometric effect and flow interference effects on the flow motion of twin rectangular cylinders in tandem, a plot of flow regimes at L^*, *AR* parameter space is portrayed in Fig. 13. In general, there are three flow regimes, i.e., overshoot regime, reattachment regime, and co-shedding regime. At all small and some medium gaps, for all *AR*s, the flow field behaves as the overshoot regime. Here, the shear layer from UC overshoots the DC and forms the vortex street with vortices of opposite sign and alternating shedding behind the DC (2S vortex). As the L^* increases, the flow field evolves toward a reattachment regime. In the reattachment regime, the shear layer of UC sheds and constantly slaps on the DC as the 2S vortex, then merges with the shear layer of DC and proceeds to shed, which enhances the fluctuation of DC. The vortex shedding from DC exhibits two parallel vortex shedding mode (P vortex) and irregular stretching vortex are detected at the far wake, which indicates the intensity of the vortex development is weaker at the far wake. The co-shedding regime occurs at most large gaps with the gap flow, and the wake flow of DC is well developed. With the increase in *AR*, the flow field form gradually transitions to the reattachment regime ($L^* = 8.0$, $AR = 2.0$). In addition, distorted stretched vortices are

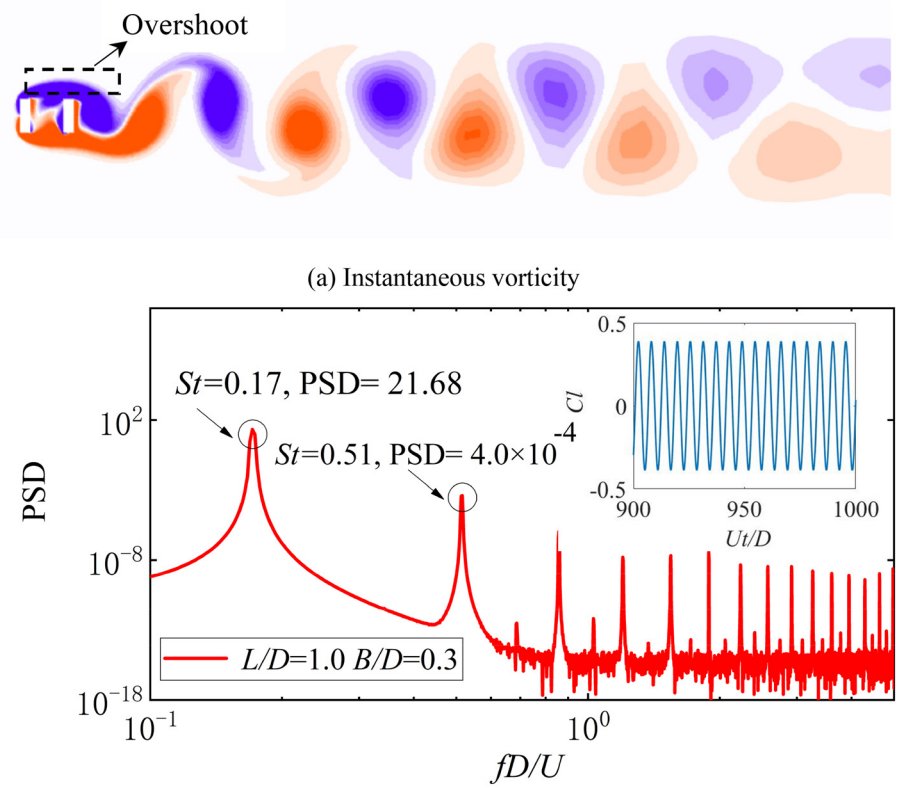

FIG. 10. Flow characteristics for $L^* = 1.0$, $AR = 0.3$. (a) Instantaneous vorticity and (b) power spectrum density (PSD) and lift coefficient time history of the downstream cylinder.

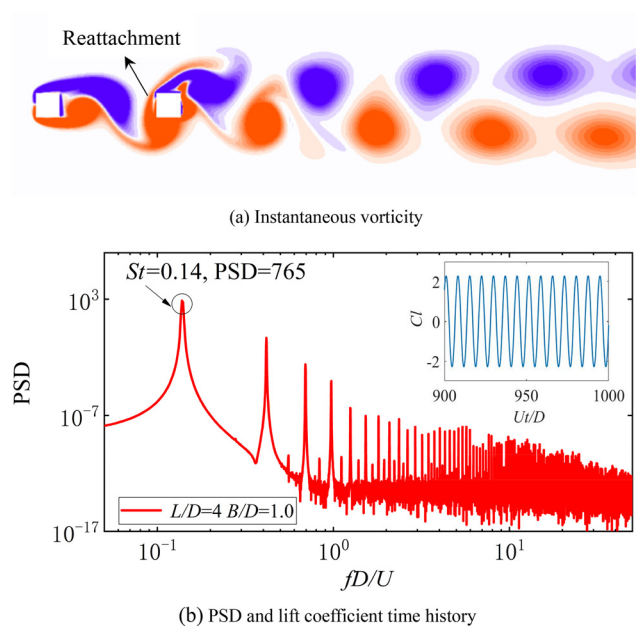

FIG. 11. Flow characteristics for $L^* = 4.0$, $AR = 1.0$. (a) Instantaneous vorticity and (b) power spectrum density (PSD) and lift coefficient time history of the downstream cylinder.

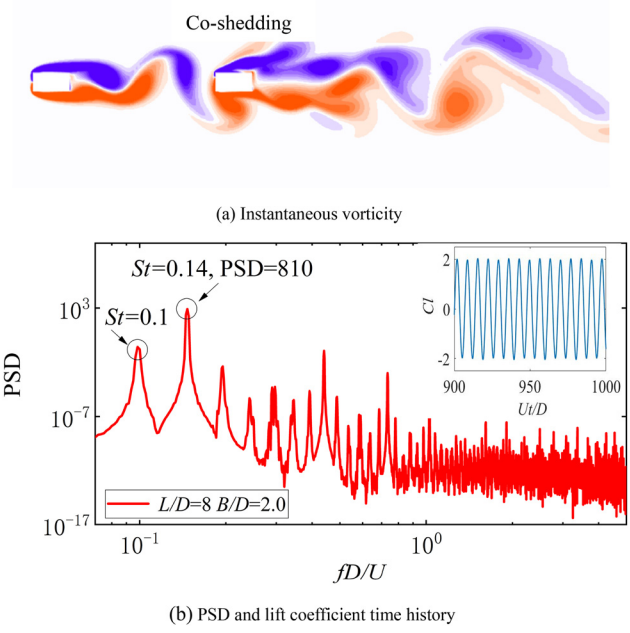

FIG. 12. Flow characteristics for $L^* = 8.0$, $AR = 2.0$. (a) Instantaneous vorticity and (b) power spectrum density (PSD) and lift coefficient time history of the downstream cylinder.

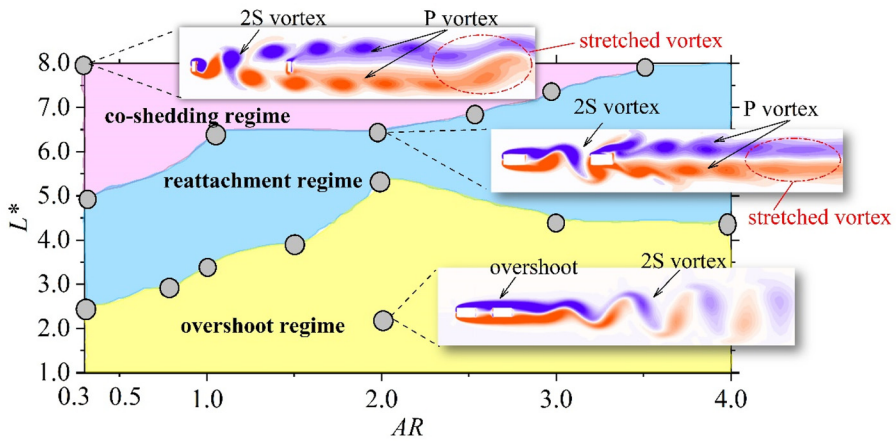

FIG. 13. Plot of flow regimes at the L^*, AR parameter space.

observed at $L^* = 8.0$, $AR = 0.3$, which implies that the vorticity field in the far wake becomes highly irregular.

D. High-order dynamic mode decomposition analysis of the flow field

To identify the main dynamic features involved in the flow of tandem twin cylinders, the HODMD method was used to study the spatial morphology and temporal evolution feature of primary modes for representative cases of $L^* = 1.0$, $AR = 0.3$ and 4, and $L^* = 4.0$, $AR = 0.3$ and 1.0, corresponding to the small and medium gaps, respectively. All data were sampled from the fully developed flow field over the twin tandem cylinders within 40 cycles of vortex shedding. For each cycle, there are 25 samples with an interval of $T/25$. Here, the dominant coherent mode features, including global mode energy and local mode form, are extracted by synchronously decomposing velocity and pressure field for the purpose of exploring their relationship with fluid forces.

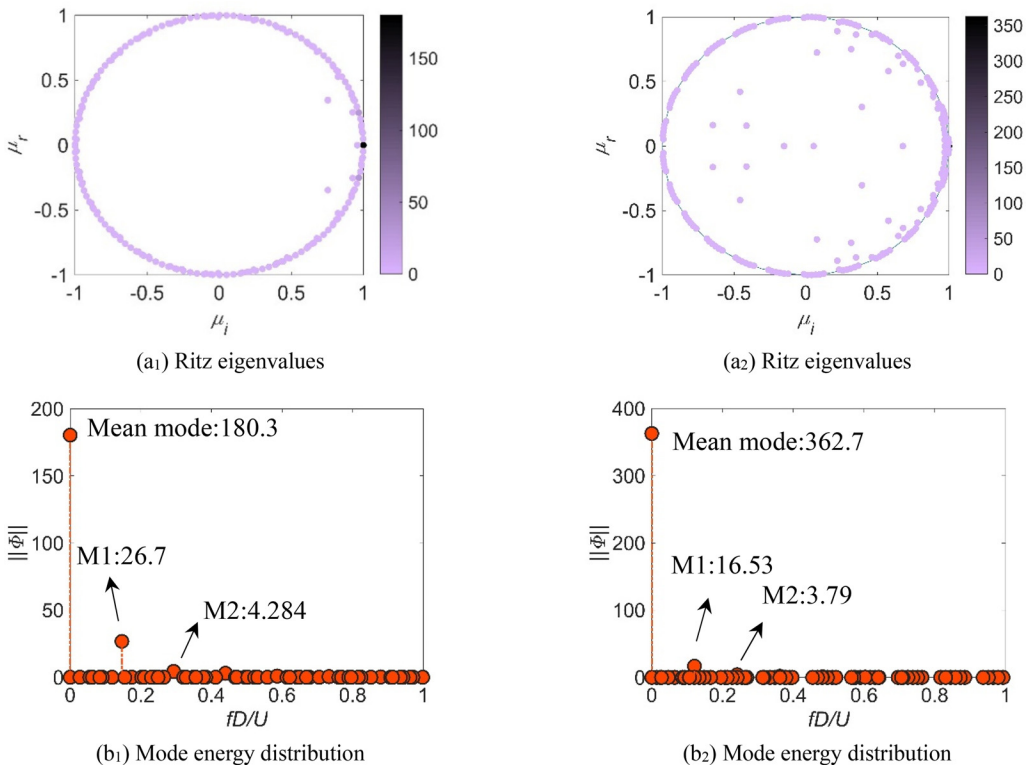

(a1) Ritz eigenvalues

(a2) Ritz eigenvalues

(b1) Mode energy distribution

(b2) Mode energy distribution

FIG. 14. Ritz eigenvalues and mode energy distribution for vorticity mode at $L^* = 1.0$, $AR = 0.3$: (a_1) and (b_1), and $L^* = 1.0$, $AR = 4$: (a_2) and (b_2).

1. $L^* = 1.0$

Figure 14 shows the calculated Ritz eigenvalues and the corresponding mode energy distributions of vorticity modes for $L^* = 1.0$, $AR = 0.3$ and $L^* = 1.0$, $AR = 4$. As expected, the eigenvalues of the dominant modes, Ritz, are basically all clustered around the unit circle, which implies that the dynamics settles on an attractor,[52] as shown in Figs. 14(a_1) and 14(a_2). In Figs. 14(b_1) and 14(b_2), the largest mode energy is seen at $fD/U = 0$, which represents the time-averaged flow field. Figures 14(b_1) and 14(b_2) illustrate that the flow regime is governed by one primary mode (mode 1) and one superharmonic mode (mode 2), and the energy of mode 2 is significantly lower than that of mode 1, which is consistent with the phenomenon shown in Fig. 10(b). A striking feature presented in Figs. 14(b_1) and 14(b_2) is that the variation of AR makes a significant difference in the energy of the modes. As the AR increases from 0.3 to 4, the energy of the mean mode (with $fD/U = 0$) increases more than twice (from 180.3 to 362.7), the energy of mode 1 decreases by 38.1% (from 26.7 to 16.53), and the energy of mode 2 also decreases. This indicates the long afterbody stabilizes the vortex shedding to some extent.

According to the values of dimensionless frequencies, the first two modes in Fig. 15 are ranked as modes 1 and 2 for $L^* = 1.0$, $AR = 0.3$ and $L^* = 1.0$, $AR = 4$. It can be noted that mode 1 is symmetrical about the centerline of twin cylinders (large-scale vortex shedding alternately in reverse), whereas mode 2 appears to be antisymmetric (antisymmetric vortex pairs from the top to the bottom, with alternating symbols in the downstream direction). In Figs. 15(a_1) and 15(b_1), the vorticity intensity of mode 1 with $AR = 4$ is reduced compared to that of $AR = 0.3$, and no vorticity appears in the gap. As a result, the fluctuating intensity of the large-scale vortex generated on the cylinders is relatively small. On the other hand, from Figs. 15(a_2) and 15(b_2), the intensity of the small-scale vortex fluctuation in the far wake region is larger for $AR = 4$ compared to $AR = 0.3$, which indicates that the flow field at the downstream region is more chaotic.

To quantitatively study the lift-and-drag forces on the surface of the twin cylinders, pressure mode diagrams and line plots are presented in Figs. 16 and 17. As can be seen from Fig. 16, the pressure mode and the vortex mode have opposite symmetry features. For mode 1 in Figs. 16(a_1) and 16(b_1), the pressure on the upside and downside of twin cylinders is in the same phase but with opposite values; thus, the sum of the pressure on two sides is 0, and this can also be found in Fig. 17(a), which implies there is a high lift force and no drag force acting on twin cylinders. For mode 2 in Figs. 16(a_2) and 16(b_2), the pressure on the upside and downside of the twin cylinders are identical including both the value and the sign; thus, the lift force is 0 and the drag force reaches a maximum. Evidently, at $AR = 4$, no gap vortex and only weak pressure on the twin cylinders' surface are detected, as shown in Fig. 17, and this further verifies the conclusion previously obtained in Figs. 9(a) and 9(c) that both lift and drag forces on the DC decrease as the AR increases to 4. In Fig. 17(a), it can be seen from mode 1 that the pressure on S2 and S4 on the DC increases gradually along the streamwise direction, which is related to the attachment and motion of the surface shear layer. Nevertheless, it is noteworthy that the pressure variations of S2 and S4 on the UC are insignificant, due to the enhanced vorticity by strong interaction between gap flow and DC, especially for $AR = 0.3$, see

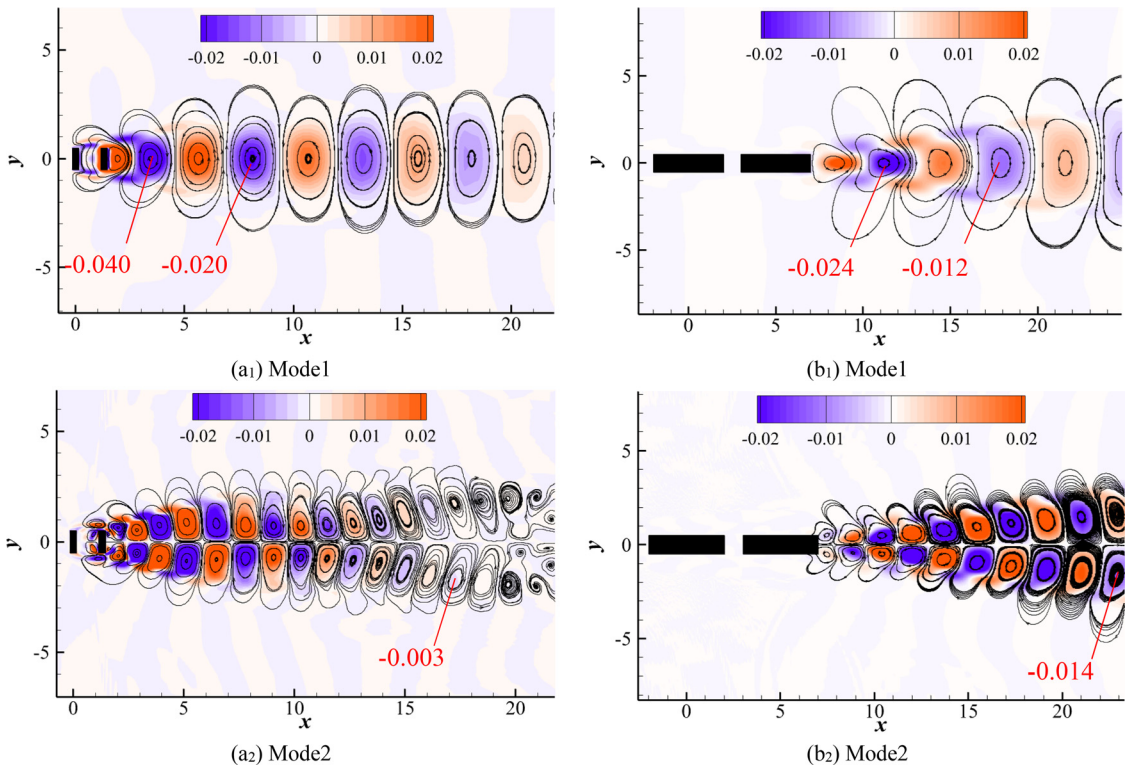

FIG. 15. Vorticity modes for $L^* = 1.0$, $AR = 0.3$: (a_1) and (a_2); vorticity modes for $L^* = 1.0$, $AR = 4$: (b_1) and (b_2).

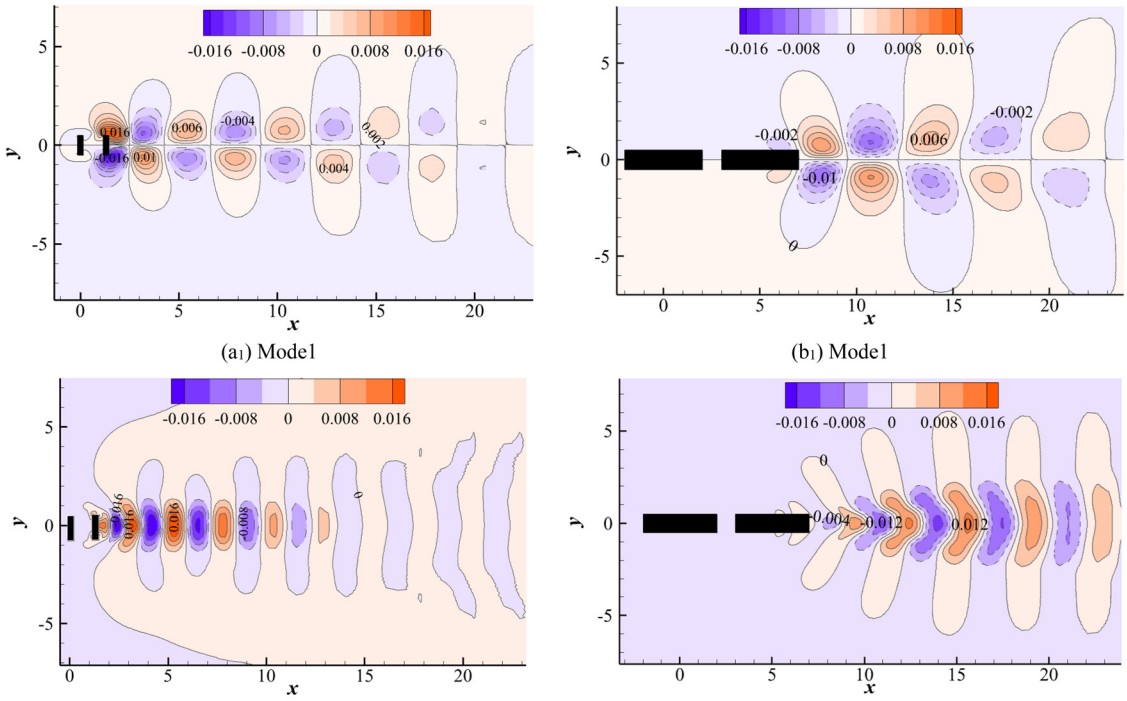

FIG. 16. Pressure modes for $L^* = 1.0$, $AR = 0.3$: (a_1) and (a_2); pressure modes for $L^* = 1.0$, $AR = 4$: (b_1) and (b_2).

Figs. 15(a_1) and 15(a_2). In addition, the combined interaction of vortex shedding of twin cylinders leads to an increase in *Cd* of DC, see Fig. 17(b).

2. $L^* = 4.0$

The HODMD method was also carried out for $L^* = 4$, using the identical configuration as for $L^* = 1$. Figure 18 displays the Ritz values computed from the u velocity and v velocity and corresponding normalized modal magnitude Φ for $L^* = 4.0$, $AR = 0.3$ and $L^* = 4.0$, $AR = 1$, which presents the distribution of the global energy at different frequencies. The corresponding dominant first two orders of vortex modes (mode 1 and mode 2) are shown in Fig. 19. Similar to $L^* = 1.0$, almost all the Ritz values are located inside the unit circle for $AR = 0.3$ and $AR = 1$; however, the variation of mode energy values is strikingly different. For $AR = 0.3$ in Fig. 18(b_1), the subharmonic M2 is observed, which indicates the presence of low-frequency large-scale

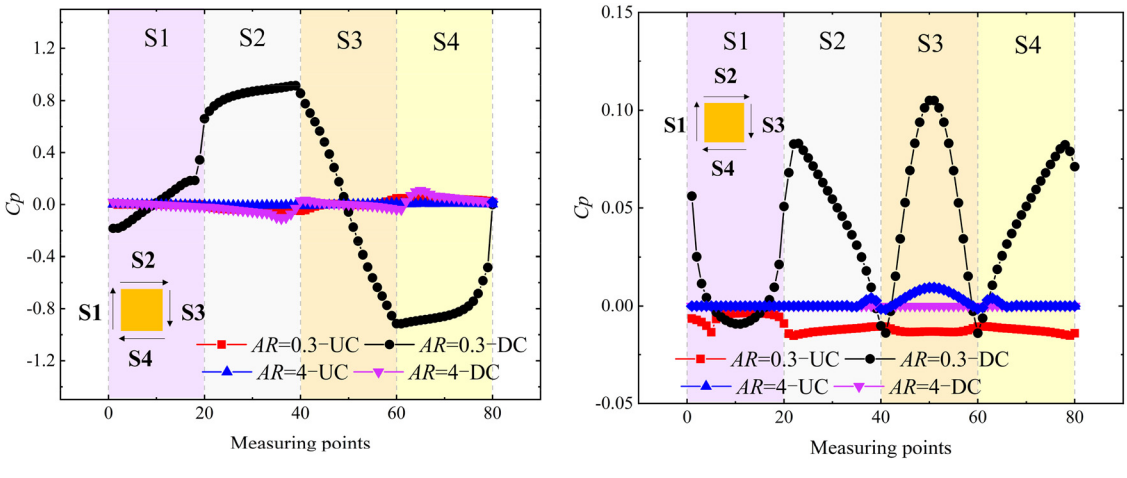

FIG. 17. Pressure distribution on the surface of the twin cylinder for M1: (a) and M2: (b).

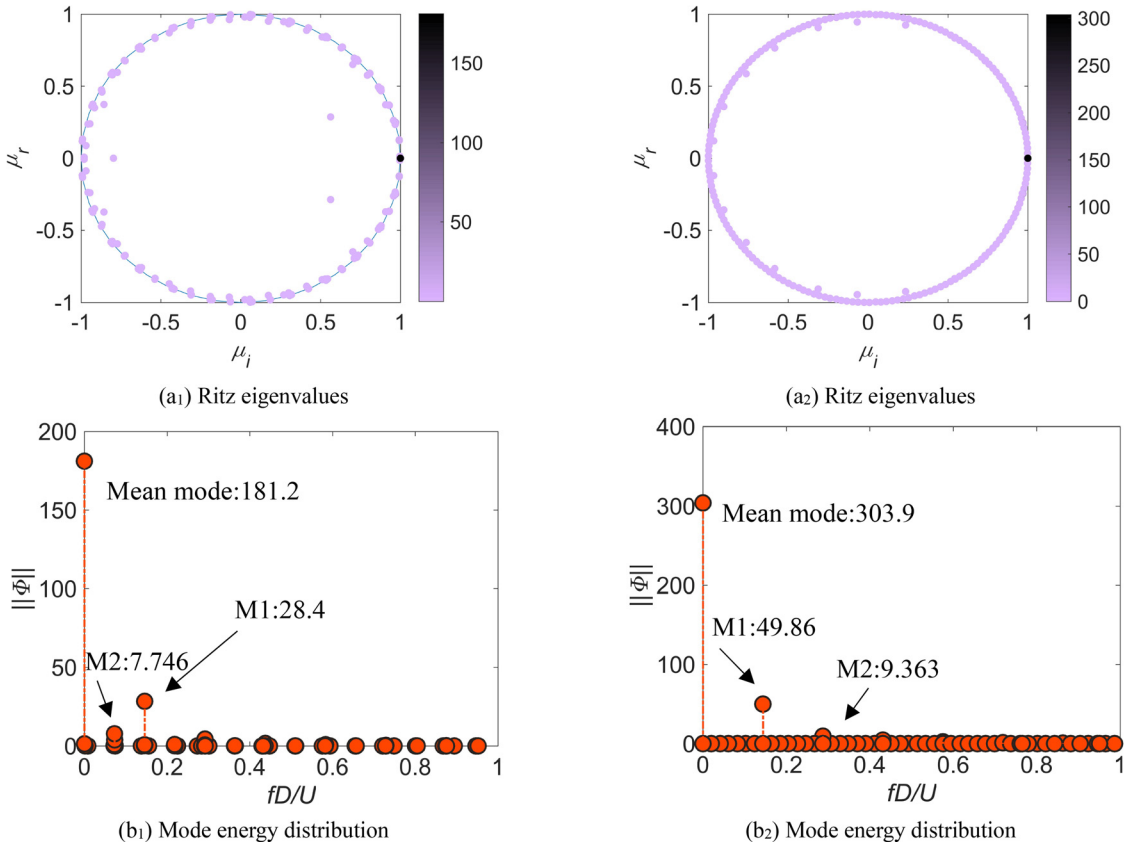

FIG. 18. Ritz eigenvalues and mode energy distribution for vorticity mode at $L^* = 4.0$ $AR = 0.3$: (a_1) and (b_1), and $L^* = 4.0$ $AR = 1$: (a_2) and (b_2).

vortices, which is consistent with Fig. 19(a_2). As the AR increases from 0.3 to 1.0, the energy of dynamic mode (mode 1 and mode 2) increases and the superharmonic disappears, which implies an increase in the fluctuation of the small-scale vortices. Also, the increment in mean mode energy of $fD/U = 0$ indicates the enhancement of the drag, especially for DC, as shown in Figs. 9(b) and 9(d). This implies the diminished shielding effect of UC is a result of increasing AR.

Figures 20 and 21 show the first two orders of pressure mode distribution and the corresponding pressure coefficients maps for the surface of twin cylinders, respectively. In Fig. 19(a_1), it is obvious that a transition of vortex shedding occurs in the medium gap for $AR = 0.3$. That is, two single vortices shed at the wake of UC (2S vortex pattern), and then gradually separate into parallel vortex (P vortex mode), which move along the downstream direction and bypass the DC. Therefore, the variations of the mode pressure on the surfaces of S2 and S4 of DC are small, see Fig. 21(a). Meanwhile, the vortex of the wake of DC is attracted to the P vortex, which contributes to reducing the fluctuation of the wake of DC. As the P vortex moves downstream, the strength of the vortex gradually diminishes and the far wake region of the DC is dominated by the large-scale Karman vortex street, see Fig. 19(a_2); thus, the mode 2 pressure on the S3 surface of DC is very small. Moreover, Fig. 21(a) shows the sharp pressure change from the S2 to S4 surface of UC for model of $AR = 0.3$ due to the flow separation and the shear layer migration. Interestingly, for $AR = 0.3$, the model pressure on the DC from S2 to S4 is less than that of the UC, while for $AR = 1$, the phenomenon is reversed, implying that the gap flow increases the fluid force on the DC and confirming the above finding; that is, as AR increases from 0.3 to 1, the UC shielding effect decreases.

For $AR = 1.0$, due to the longer afterbody, the size of gap vortices is decreased, and vortices cannot be separated by DC like $AR = 0.3$. Instead, strong interactions can be observed in the gaps of Figs. 19(b1) and 19(b2), and alternating vortex shedding (as 2S vortex pattern) near the wake of DC can be seen by mode 1. Interestingly, the evolution of the 2S vortex to the P vortex is observed in the far wake region, which indicates the dissipation of fluctuation energy. Moreover, Fig. 19(b2) exhibits the dominance of small-scale vortices in the flow field, which implies the increase in fluctuation components and the complexity of the flow field. Furthermore, comparing the flow field modes with $AR = 1.0$ and 0.3, it shows that the mode transition of the gap flow is responsible for the reduced accuracy of the forces predicted by CNN-HODMD, as shown in Fig. 7. In Fig. 21(b), pressure fluctuation occurs at the trailing edge of S2 and S4 of the DC, which is due to the small-scale vortices on upside and downside of the DC in Fig. 19(b_2). However, the pressure on the S3 of the DC is reduced, as a result of the fact that the vortices immediately behind the DC have opposite

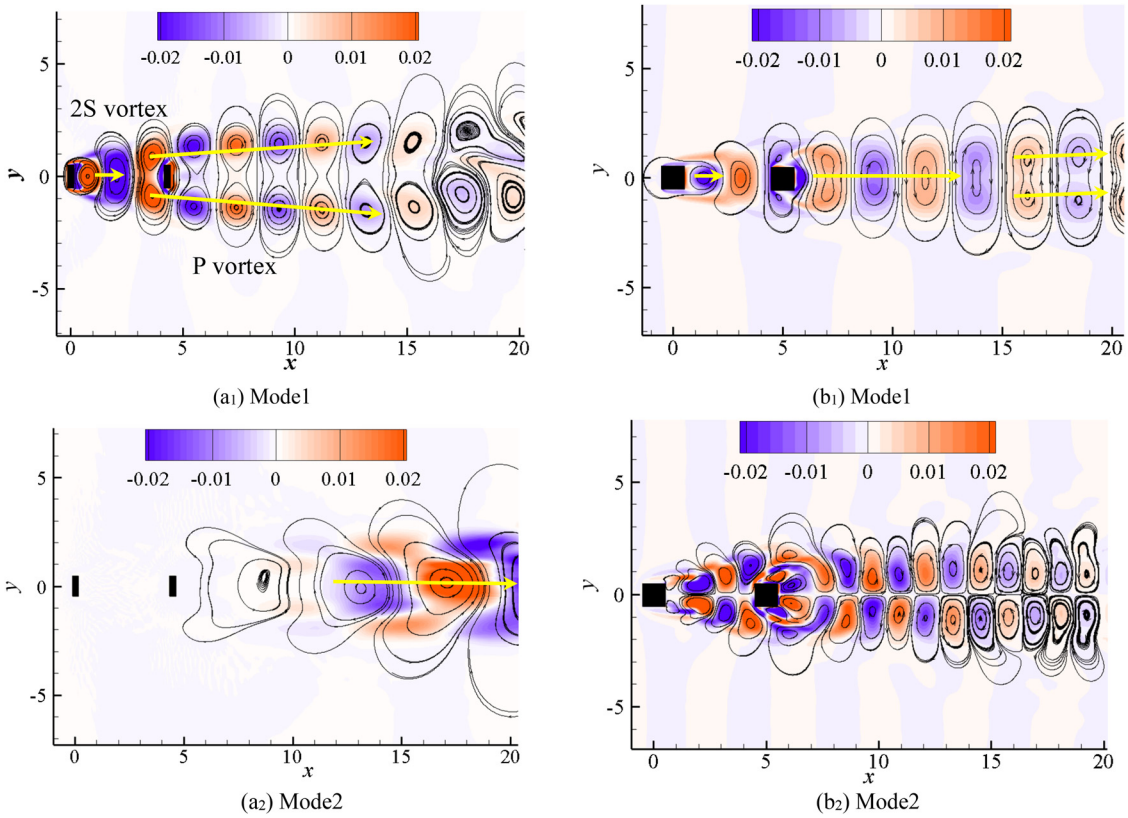

FIG. 19. Vorticity modes for $L^* = 4.0$ $AR = 0.3$: (a_1) and (a_2); vorticity modes for $L^* = 4.0$ $AR = 1$: (b_1) and (b_2).

signs to those of the side vortices (S2 and S4), so that the fluctuation energy is gradually consumed.

V. CONCLUSION

In this study, flow past twin rectangular cylinders in a tandem arrangement with different gap space and aspect ratios were simulated at a Reynolds number of 150 by DNS. The gap ratio L^* varies from 1 to 8, and the aspect ratio AR is selected from 0.3 to 4. A new surrogate model, based on the convolutional neural network and higher-order dynamic modal (CNN-HODMD), is developed for the prediction of the unsteady fluid force of twin cylinders under different AR and L^*. Specifically, the dimensionality of the original matrix, i.e., time history of lift force, is augmented by Taken's embedding theorem, mode reduction is then used to decompose the mode coefficients and exploit the low-dimensional linear representation, and finally, deep learning is deployed to map the relationship between input geometrical parameter and output reduced mode coefficient. To understand the correspondence between load feature and flow field particularly for twin tandem cylinders, the effect of side ratio and gap distance on both the fluid force and flow structure is investigated. More importantly, the pressure and velocity fields are synchronously analyzed via HODMD. The main findings are summarized below.

(1) The prediction of the mode coefficients by the CNN-HODMD model was first investigated, and the results showed that the RMSE values were within 0.01, which indicates a high prediction accuracy. In addition, the accuracy of predicted mode coefficients for $AR > 1$ is higher compared to those for $AR < 1$. The reason is that the gap flow transitions from 2S vortex pattern to P vortex pattern at $AR < 1$. For the time history of the lift force, the CNN-HODMD model can efficiently and accurately predict within 5% error, although the error varies slightly with the change in AR. The results show that the CNN-HODMD model works well in capturing the potential relationship between the lift force and the input parameters (AR and L^*) on the twin tandem cylinders.

(2) Fluid force and flow structure of the twin cylinders are closely related to L^* and AR. It was found that the vortex shedding strength of UC is quite weak for small gaps ($L^* = 1, 2$), especially for $AR > 1$ (flat cylinder). Compared to the other cases, the lift on the large aspect ratios ($AR > 1$) of DC (flat cylinder) is largely enhanced for the large gap cases ($L^* = 6, 8$). A possible reason attributing to this phenomenon is that the wake of UC with a large gap is fully produced and slapped onto the DC, which increases the fluctuating force of DC. Oppositely, the shielding effect of UC greatly reduces the drag force on the DC for all cases, yet this shielding effect is weakened as the gap increases. Moreover, it is found that the large gaps cases exhibit the sub-harmonic spectral peak but reduced primary frequency, which indicates the sizes of the large-scale vortex, is increased.

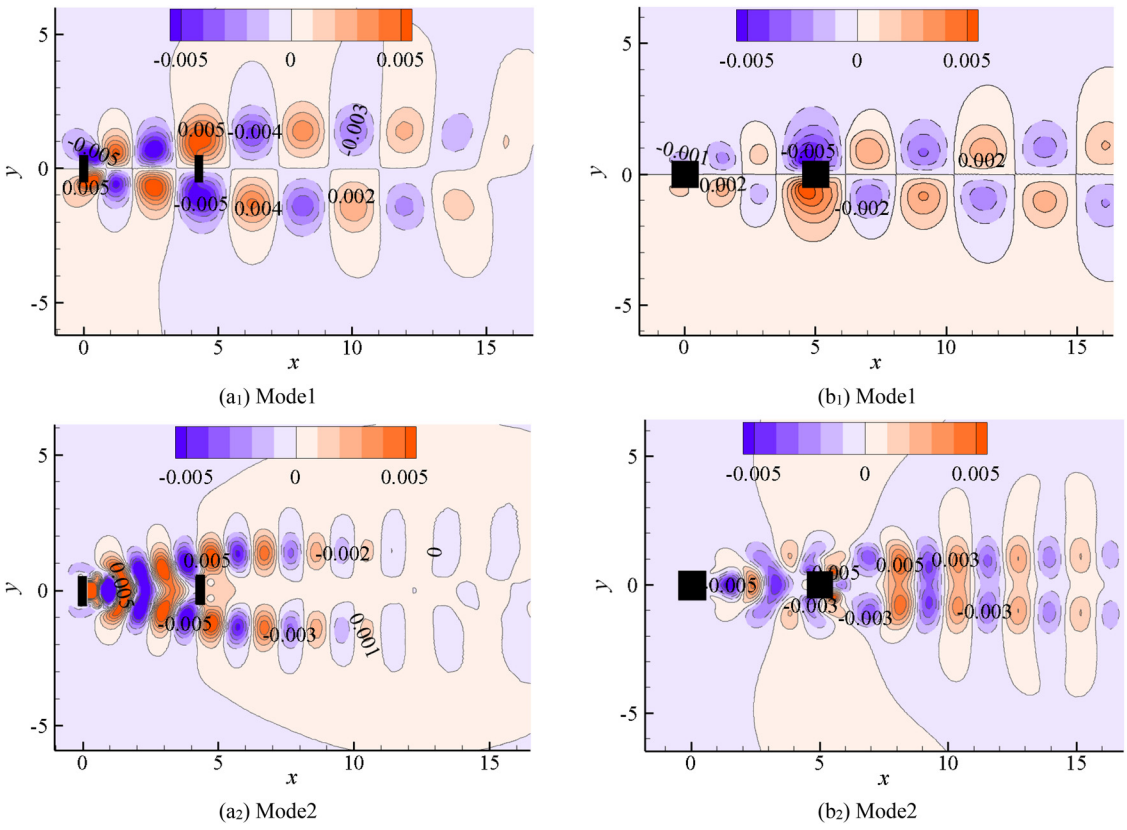

FIG. 20. Pressure modes for $L^* = 4.0$ $AR = 0.3$: (a_1) and (a_2); pressure modes for $L^* = 4.0$ $AR = 1$: (b_1) and (b_2).

(3) Based on the behavior of the shear layer, three distinct flow regimes are recognized based on *AR*s and L^*, i.e., the overshoot regime, the reattachment regime, and the co-shedding regime. In the overshoot regime, the shear layer of UC overshoots the DC and develops an alternating vortex shedding pattern (2S vortex) in the wake of DC, which occurs at all small and several medium gaps. In the reattachment regime, the 2S vortex forms behind the UC, which reattaches on the DC, and the wake of

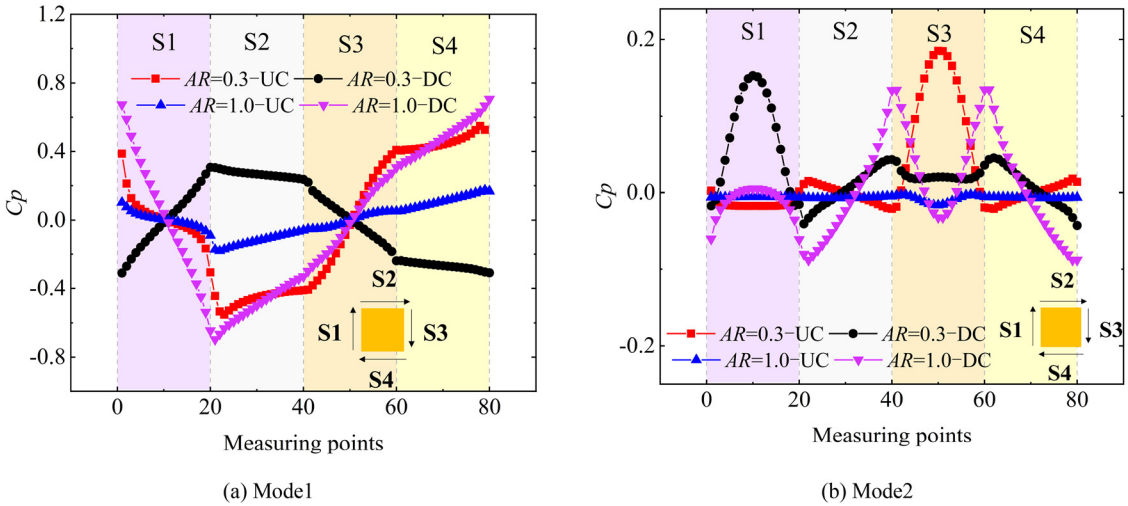

FIG. 21. Pressure distribution on the surface of the twin cylinder for M1: (a) and M2: (b).

DC also shows a 2S vortex shedding pattern. It occurs at some medium and large gaps. In the co-shedding regime, the vortex shedding develops simultaneously near the leeward of the twin cylinders; therefore, the UC always exhibits a 2S shedding pattern, while a line of parallel and stretched vortices is observed behind the DC.

(4) HODMD of the vorticity and mode pressure was conducted for two representative cases ($L^* = 1.0$, $AR = 0.3$, 4, and $L^* = 4.0$, $AR = 0.3$, 1.0) to extract the dynamic properties in the flow. It is found that the primary vorticity mode (mode 1) and a superharmonic vorticity mode (mode 2) dominate the dynamic mode, and the energy of vorticity mode 2 is much lower than vorticity mode 1. For the small gap ($L^* = 1.0$), the vorticity mode 1 and its pressure counterpart contribute high lift forces. As the AR increased from 0.3 to 4, the primary mode becomes more energetic; thus, the fluctuating component of the wake of twin cylinders is reduced. This indicates the long afterbody stabilizes the vortex shedding to some extent. Moreover, at $AR = 0.3$, the pressure of the DC is larger than that of the UC, due to the enhanced vorticity by strong interaction between gap flow and DC, which is indicated by the vorticity mode. For the medium gap ($L^* = 4.0$), as AR increases from 0.3 to 1.0, the dynamic mode energy is increased, which is quite different from that for small gaps. For $AR = 0.3$, the wake of UC transforms from 2S to P vortex pattern, bypassing DC, and attracting the wake vortex of DC into the P vortex, which reduces the fluctuation force of the DC compared to UC. For $AR = 1.0$, due to the longer afterbody, the size of gap vortices is decreased, and they cannot be divided by DC like $AR = 0.3$. Instead, they thus strongly interact with the separated shear flow of UC, which leads to an increase in the fluctuating force. In addition, the extrusion of the small-scale vortex also leads to high pressure on the upper and lower sides of the DC.

Given that the combination of reduced-order model and machine learning techniques could bring about significant computational cost reduction and can build a surrogate model that facilitates high-fidelity, efficient, and accurate load prediction. Therefore, it is feasible to generalize and popularize this modeling technique to deploy other engineering tasks that have requirements for computing resources and efficiency, including but not limited to flow control design, aerodynamic shape optimization, and other flow problems considering complex flow condition and bluff-body geometry.

ACKNOWLEDGMENTS

The authors would like to thank the support of the Natural Science Foundation of Heilongjiang Province China (Grant No. LH2020E010).

AUTHOR DECLARATIONS

Conflict of Interest

The authors have no conflicts to disclose.

Author Contributions

Tingting Liu: Formal analysis (equal); Investigation (equal); Validation (equal); Writing – original draft (equal). **Lei Zhou:** Conceptualization (equal); Formal analysis (equal); Supervision (equal); Writing – review & editing (equal). **Hui Tang:** Methodology (equal); Validation (equal). **Hongfu Zhang:** Conceptualization (equal); Funding acquisition (equal); Methodology (equal); Supervision (equal).

DATA AVAILABILITY

The data that support the findings of this study are available from the corresponding author upon reasonable request.

REFERENCES

[1]M. Lahooti and D. Kim, "Unsteady concentration transport over an array of cylinders in low-Reynolds-number flow," Phys. Fluids **32**(5), 053602 (2020).
[2]H. Zhang, L. Zhou, and K. T. Tim, "Mode-based energy transfer analysis of flow-induced vibration of two rigidly coupled tandem cylinders," Int. J. Mech. Sci. **228**, 107468 (2022).
[3]W.-Y. Chang, G. Constantinescu, and W.-F. Tsai, "Effect of array submergence on flow and coherent structures through and around a circular array of rigid vertical cylinders," Phys. Fluids **32**(3), 035110 (2020).
[4]K. Kingora, W. Burks, and H. Sadat-Hosseini, "Flow and mass transfer characteristics for interacting side-by-side cylinders," Phys. Fluids **34**(2), 023602 (2022).
[5]H. Zhang, D. Xin, J. Zhan, and L. Zhou, "Flow past a transversely oscillating cylinder at lock-on region and three-dimensional Floquet stability analysis of its wake," Phys. Fluids **33**, 025111 (2021).
[6]D. Dung, D. Nguyen, T. Nguyen Van, and I. Ngo, "Low-Reynolds-number wake of three tandem elliptic cylinders," Phys. Fluids **34**, 043605 (2022).
[7]L. Zhou, K. T. Tse, G. Hu, and Y. Li, "Higher order dynamic mode decomposition of wind pressures on square buildings," J. Wind Eng. Ind. Aerodyn. **211**, 104545 (2021b).
[8]H. Zhang, L. Zhou, T. Liu, Z. Guo, and F. Golnary, "Dynamic mode decomposition analysis of the two-dimensional flow past two transversely in-phase oscillating cylinders in a tandem arrangement," Phys. Fluids **34**, 033602 (2022).
[9]M. M. Zdravkovich, " Review of flow interference between two circular cylinders in various arrangements," J. Fluid Eng. **99**(4), 618 (1977).
[10]J. Mizushima and N. Suehiro, "Instability and transition of flow past two tandem circular cylinders," Phys. Fluids **17**(1–12), 104107 (2005).
[11]T. Tsutsui, "Experimental study on the instantaneous fluid force acting on two circular cylinders closely arranged in tandem," J. Wind Eng. Ind. Aerodyn. **109**, 46 (2012).
[12]R. Subburaj and S. Vengadesan, "Flow features for two cylinders arranged in tandem configuration near a free surface," J. Fluids Struct. **91**, 102770 (2019).
[13]P. Wang, Q. Zhou, M. M. Alam, Y. Yang, and M. Li, "Effects of streamwise gust amplitude on the flow around and forces on two tandem circular cylinders," Ocean Eng. **261**, 112040 (2022).
[14]M. M. Alam, H. Sakamoto, and Y. Zhou, "Determination of flow configurations and fluid forces acting on two staggered circular cylinders of equal diameter in cross-flow," J Fluids Struct **21**(4), 363 (2005).
[15]D. Sumner, "Two circular cylinders in cross-flow: A review," J. Fluid Struct. **26**(6), 849 (2010).
[16]L. Zhou, H. Li, K. Tim, X. He, G. Y. C. Maceda, and H. Zhang, "Sensitivity-aided active control of flow past twin cylinders," Int. J. Mech. Sci. **242**, 108013 (2003).
[17]M. Mahbub Alam and Y. Zhou, "Phase lag between vortex shedding from two tandem bluff bodies," J. Fluid Struct. **23**(2), 339 (2007).
[18]L. Wang and Y. Zhou, "Two tandem cylinders of different diameters in cross-flow: Effect of an upstream cylinder on wake dynamics," J. Fluid Mech. **836**(5), 5 (2018).
[19]M. Zhao, A.-A. Mamoon, and H. Wu, "Numerical study of the flow past two wall-mounted finite-length square cylinders in tandem arrangement," Phys. Fluids **33**(9), 093603 (2021).
[20]X. Du, H. Xu, W. Ma, C. Dai, and Q. Liu, "Experimental study on aerodynamic characteristics of two square cylinders at various incidence angles," J. Wind. Eng. Ind. Aerodyn. **191**, 154 (2019).

[21]M. M. Zdravkovich, "The effects of interference between circular cylinders in cross flow," J. Fluid Struct. **1**(2), 239 (1987).
[22]A. Sohankar, "A LES study of the flow interference between tandem square cylinder pairs," Theor. Comput. Fluid Dyn. **28**(5), 531 (2014).
[23]W. Zhang, H.-S. Dou, Z. Zhu, and Y. Li, "Unsteady characteristics of low-Re flow past two tandem cylinders," Theor. Comput. Fluid Dyn. **32**(4), 475 (2018).
[24]J. Shang, Q. Zhou, M. Alam, H. Liao, and S. Cao, "Numerical studies of the flow structure and aerodynamic forces on two tandem square cylinders with different chamfered-corner ratios," Phys. Fluids **31**(7), 075102 (2019).
[25]Md. Mahbub Alam, "The aerodynamics of a cylinder submerged in the wake of another," J. Fluid Struct. **51**, 393 (2014).
[26]Y. Zhou and M. Mahbub Alam, "Wake of two interacting circular cylinders: A review," Int. J. Heat Fluid Flow **62**, 510 (2016).
[27]T. Igarashi, "Characteristics of the flow around two circular cylinders arranged in tandem: 1st report," Bull. JSME **24**(188), 323 (1981).
[28]T. Igarashi, "Characteristics of the flow around two circular cylinders arranged in tandem: 2nd report, unique phenomenon at small spacing," Bull. JSME **27** (233), 2380 (1984).
[29]L. Ljungkrona, C. Norberg, and B. Sundén, "Free-stream turbulence and tube spacing effects on surface pressure fluctuations for two tubes in an in-line arrangement," J. Fluid Struct. **5**(6), 701 (1991).
[30]W. Yang and M. A. Stremler, "Critical spacing of stationary tandem circular cylinders at Re ≈ 100," J. Fluid Struct. **89**, 49 (2019).
[31]M. M. Alam and J. P. Meyer, "Global aerodynamic instability of twin cylinders in cross flow," J Fluids Struct. **41**,135 (2013).
[32]X. Hu, X. Zhang, and Y. You, "On the flow around two circular cylinders in tandem arrangement at high Reynolds numbers," Ocean Eng. **189**, 106301 (2019).
[33]A. Mashhadi and A. Sohankar, "Flow over rectangular cylinder: Effects of cylinder aspect ratio and Reynolds number," Int. J. Mech. Sci. **195**, 106264 (2021).
[34]R. T. Gon ç alves, G. R. Franzini, G. F. Rosetti, J. R. Meneghini, and A. L. C. Fujarra, "Flow around circular cylinders with very low aspect ratio," J. Fluid Struct. **54**, 122 (2015).
[35]C. Norberg, "An experimental investigation of the flow around a circular cylinder: Influence of aspect ratio," J. Fluid Mech. **258**, 287 (1994).
[36]X. Wu, F. Chen, and S. Zhou, "Stationary and flow-induced vibration of two elliptic cylinders in tandem by immersed boundary-MRT lattice Boltzmann flux solver," J. Fluid Struct. **91**, 102762 (2019).
[37]Z. ul Islam, S. ul Islam, and C. Y. Zhou, "The wake and force statistics of flow past tandem rectangles," Ocean Eng. **236**, 109476 (2021).
[38]K. Hammad and I. Milanovic, "A POD study of an impinging jet flowfield," *Proceedings of the ASME 2009 Fluids Engineering Division Summer Meeting* (ASME, 2009), Vol. 1, p. 1477.
[39]P. Huan, H. Zhu, K. Zhang, D. Zhou, Y. Bao, Y. Xu, and Z. Han, "Dynamic mode decomposition based analysis of flow past a transversely oscillating cylinder," Phys. Fluids **33**, 033604 (2021).
[40]P. Schmid and J. Sesterhenn, "Dynamic mode decomposition of numerical and experimental data," J. Fluid Mech. **656**, 28 (2008).
[41]S. L. Clainche and J. Vega, "Higher order dynamic mode decomposition to identify and extrapolate flow patterns," Phys. Fluids **29**, 084102 (2017).
[42]Y. Bao, Q. Wu, and D. Zhou, "Numerical investigation of flow around an inline square cylinder array with different spacing ratios," Comput. Fluids **55**, 118 (2012).
[43]R. Nepali, H. Ping, Z. Han, D. Zhou, H. Yang, J. Tu, Y. Zhao, and Y. Bao, "Two-degree-of-freedom vortex-induced vibrations of two square cylinders in tandem arrangement at low Reynolds numbers," J. Fluid Struct. **97**, 102991 (2020).
[44]N. Erichson, L. Mathelin, Z. Yao, S. Brunton, M. Mahoney, and J. Kutz, "Shallow neural networks for fluid flow reconstruction with limited sensors," Proc. R. Soc. A **476**, 20200097 (2020).
[45]W. Yuqi, Y. Wu, L. Shan, Z. Jian, R. Huiying, Y. Tiechui, and K. Menghai, "Flow field reconstruction method based on array neural network," Aeronaut. J. **125**(1283), 223 (2021).
[46]Y. Liu, Y. Lu, Y. Wang, D. Sun, L. Deng, F. Wang, and Y. Lei, "A CNN-based shock detection method in flow visualization," Comput. Fluids **184**, 1 (2019).
[47]Y. Zhao, X. Zhao, and Y. Meng, "Prediction of confined flow field around a circular cylinder and its force based on convolution neural network," IEEE Access **10**, 6889 (2021).
[48]Y. Afshar, S. Bhatnagar, S. Pan, K. Duraisamy, and S. J. C. M. Kaushik, "Prediction of aerodynamic flow fields using convolutional neural networks," Comput. Mech. **64**, 525 (2019).
[49]T. P. Miyanawala and R. Jaiman, "An efficient deep learning technique for the Navier–Stokes equations: Application to unsteady wake flow dynamics," arXiv:1710.09099 (2017).
[50]A. Sohankar, "A numerical investigation of the flow over a pair of identical square cylinders in a tandem arrangement," Int. J. Numer. Meth. Fluids **70** (10), 1244 (2012).
[51]F. Nikfarjam and A. Sohankar, "Study of hysteresis associated with power-law fluids past square prisms arranged in tandem," Ocean Eng. **104**, 698 (2015).
[52]I. Mezić, "Analysis of fluid flows via spectral properties of the Koopman operator," Annu. Rev. Fluid Mech. **45**(1), 357 (2013).